Metabolomics assisted with stable-isotope labeling: exploring neuronal metabolism related to Parkinson's disease

Huang, L.

Chapter 4:

Reconstruction of glutathione metabolism in neuronal model of rotenone-induced neurodegeneration using mass isotopologue analysis with HILIC-Zeno MRM^{HR}

Based on:

Luojiao Huang, Nicolas Drouin, Jason Causon, Agnieszka Wegrzyn, Jose Castro-Perez, Ronan Fleming, Amy Harms, and Thomas Hankemeier*

Reconstruction of Glutathione Metabolism in the Neuronal Model of Rotenone-Induced Neurodegeneration Using Mass Isotopologue Analysis with Hydrophilic Interaction Liquid Chromatography-Zeno High-Resolution Multiple Reaction Monitoring

Analytical Chemistry 2023; DOI: 10.1021/acs.analchem.2c04231

Abstract

Accurate reconstruction of metabolic pathways is an important prerequisite for interpreting metabolomics changes and understanding the diverse biological processes in disease models. A tracer-based metabolomics strategy utilizes stable isotope-labeled precursors to resolve complex pathways by tracing the labeled atom(s) to downstream metabolites through enzymatic reactions. Isotope enrichment analysis is informative and achieved by counting total labeled atoms and acquiring the mass isotopologue distribution (MID) of the intact metabolite. However, quantitative analysis of labeled metabolite substructures/moieties (MS^2 fragments) can offer more valuable insights into the reaction connections through measuring metabolite transformation. In order to acquire the isotopic labeling information at the intact metabolite and moiety level simultaneously, we developed a method that couples hydrophilic interaction liquid chromatography (HILIC) to Zeno trap-enabled high-resolution multiple reaction monitoring (MRM^{HR}). The method enabled accurate and reproducible MID quantification for intact metabolites as well as their fragmented moieties, with notably high sensitivity in the MS^2 fragmentation mode based on the measurement of ^{13}C or ^{15}N-labeled cellular samples. The method was applied to human induced pluripotent stem cell-derived neurons to trace the fate of $^{13}C/^{15}N$ atoms from D-$^{13}C_6$-glucose/L-$^{15}N_2$-glutamine added to the media. With the MID analysis of both intact metabolites and fragmented moieties, we validated the pathway reconstruction of de novo glutathione synthesis in mid-brain neurons. We discovered increased glutathione oxidization from both basal and newly synthesized glutathione pools under neuronal oxidative stress. Furthermore, the significantly decreased de novo glutathione synthesis was investigated and associated with altered activities of several key enzymes, as evidenced by suppressed glutamate supply via glucose metabolism and a diminished flux of glutathione synthetic reaction in the neuronal model of rotenone-induced neurodegeneration.

Introduction

A metabolic network is a (sub)set of metabolic biochemical reactions known to take place in a living organism.[1] Metabolomics studies quantitative changes in metabolite levels and can provide valuable insights into the understanding of disease origin, progression and prognosis, as well as the effects and mechanism of pharmacological interventions.[2,3] Metabolomics studies of Parkinson's disease (PD) have suggested that energetic failure and increased oxidative stress are significant metabolic hallmarks in the neurodegeneration process.[4,5] However, metabolic network robustness poses a challenge to the identification of pathway activities in response to perturbations[6,7] because changes in metabolite consumption and production may not be accompanied by metabolite concentration changes. It is also difficult to distinguish between de novo synthesis and recycling of the existing metabolite pool, which reflects the activity of different metabolic pathways.

Isotope tracing techniques allow one to trace the incorporation of heavy atoms (stable or radioactive[8]) into downstream intermediates from a given labeled precursor. It is an excellent way to monitor pathway activity and has been successfully applied to different levels of organism studies, such as ex-vivo tissues,[9,10] in-vivo animal models[9–11] and in-vitro cellular culture[12]. Mass spectrometry (MS) has become the principal technique used for the analysis of stable isotope-labeled metabolites. It requires only a small amount of sample, manifests excellent detection sensitivity, and can provide structural information on multiple compounds simultaneously. Labeled distributions of intact molecules can be obtained via MS measurements, which consist of a set of mass isotopologue abundances. Mass isotopologue distribution (MID) analysis at the MS^1 level has been generally used in tracer-based metabolomics studies for tracing labeled enrichment through intermediates and probing pathway activity.[13–16] Subsequently, more attention has been paid to acquiring substructural information on labeled isotopologues and improving metabolic flux interpretation.[17,18]

Tandem MS-based approaches, using multiple reaction monitoring (MRM), can reveal the isotope labeling states of selected precursor and product ions by including all possible combinations in the transition pairs.[9,19–21] This method is popular for achieving good performance in metabolite quantification. However, it still shows technical drawbacks in measuring stable isotope-labeled metabolites in a broader metabolomic scope. The number of transition pairs considerably increases with an increasing metabolite atom number, leading to a longer cycle time and fewer data points per peak, as well as less accurate quantification and lower sensitivity for low-abundance isotopologues. In the case for phosphorylated metabolites, compared to PO_3^- or $H_2PO_4^-$ ions, carbon-containing product ions carry more structural information and are more useful for atom tracing over intersecting

pathways. However, they are generally in very low abundance, which requires a longer dwell time for each transition pair to reach good sensitivity.[22]

To overcome these difficulties, advanced tandem MS-based approaches have been developed recently. The MRM methods on triple quadrupole instruments with dynamic modification of the mass filter resolution for precursor or product ions can effectively minimize total MRM transitions, enabling the detection of intact and fragmented metabolite isotopologues with good quantification accuracy in two separate runs.[22] Based on a quadrupole linear ion trap instrument, a new liquid chromatography (LC)−mass spectrometry (MS)/MS acquisition method, and a novel isotope recapitulation algorithm (MID Max), the coverage of intact and fragmented metabolite isotopologues has been further extended by combining MRM and an enhanced data-dependent product ion scan type in a single run.[23] Parallel reaction monitoring (PRM) based on high-resolution MS was able to obtain intact and fragmented isotopologue distributions in high resolution within a single analytical run, resulting in a significantly lower cycle time compared to MID Max.[24] Other tandem MS-based approaches in high resolution via data-independent acquisition techniques are also available, such as SWATH fragmentation over stacked mass isolation windows on a QqTOF MS[25-27] and all-ion fragmentation within a wide, predefined mass window on an Orbitrap Fusion Tribrid MS[28]. When using the SWATH technique, erroneous MID quantification was found for precursors positioned on the margins of two neighboring windows.[26] This requires special attention to properly design Q1 isolation windows for target metabolite quantification. Jaiswal et al. suggested employing two different SWATH programs to achieve good MID quantifications corresponding to 19 intermediate metabolites by ensuring all precursor isotopologues fall into a single window in one of the programs.[26,29] Compared to PRM, the co-fragmentation of all isotopologues of certain metabolite in a single mass window showed higher sensitivity in quantifying precursor and fragment isotopologues of low abundance.[29] However, there is no direct spectral connection between a precursor and its corresponding fragments, making it difficult to determine the detailed positioning of labeled atoms within a particular precursor isotopologue. This type of tandem isotopologue distribution, to be noted, has shown strong benefits for improving metabolic flux analysis.[30,31]

Metabolic pathway reconstruction of central carbon metabolism and its connected de novo synthesis pathways is critical for understanding the consecutive reaction changes from energy failure towards oxidative stress in Parkinson's disease. Therefore, to facilitate reconstructing metabolite transformations along these pathways and offer a comprehensive picture of metabolic regulation using both intact and fragmented metabolite isotopologues, we need high-sensitivity detection, but also high data quality for structural elucidation of

the MS^2 spectra. In this work, we present hydrophilic interaction liquid chromatography (HILIC)−multiple reaction monitoring (MRM^{HR}) using Zeno trap pulsing, a recently introduced system of trapping fragment ions prior to the time-of-flight (TOF) injection. This method combines the advantages of HILIC for wide coverage of polar metabolome analysis and the Zeno trap-enabled technique for duty cycle improvement.[32] We compared the performance of the Zeno method to that of the SWATH method and MRM^{HR} (general PRM) with regards to the aspects of sensitivity, accuracy, and fragmentation reproducibility in MID analysis. We further applied the HILIC-Zeno MRM^{HR} method to a classic neuronal model of rotenone-induced neurodegeneration and revealed diverse flux regulations via glucose and glutamine metabolism into glutathione metabolism related to neurodegeneration.

Materials and methods

1. Chemicals and reagents

Standards were purchased from Sigma-Aldrich (Zwijndrecht, The Netherlands) and Fluka (Seelze, Germany). The tracer substances D-$^{13}C_6$-Glucose (99% isotopic purity) and L-$^{15}N_2$-glutamine (98% isotopic purity) were purchased from Cambridge Isotope Laboratories (Tewksbury, MA, USA). Acetonitrile in LC-MS grade and chloroform in HPLC grade were purchased from Biosolve B.V. (Valkenswaard, The Netherlands). Methanol in Ultra-LC-MS grade was purchased from ActuAll (Oss, The Netherlands). Milli-Q Ultra-pure water was obtained from a Merck Milli-pore A10 purification system (Raleigh, USA). Ammonium formate (≥99.995% trace metals basis) and rotenone were purchased from Sigma-Aldrich (Zwijndrecht, The Netherlands). Ammonium hydroxide (28-30 wt% solution of ammonia in water) was purchased from Acros Organics (Geel, Belgium).

2. Standard solutions and cell culture medium

Individual stock solutions of 40 standards were made with 50% MeOH or pure water in 1 mg/mL and stored in -80 ℃ (Table S1). Mixed standard solutions were prepared at the concentrations of 20, 15, 10, 7.5, 5.0, 2.5, 1.25, 0.5 and 0.1 μg/mL with 50% MeOH as the dilution solution. According to an adapted protocol from Reinhardt,[33,34] a basal neuron culture medium, N2B27, was made by mixing equal amounts of neurobasal medium (Invitrogen/Life Technologies) and Dulbecco's modified Eagle's medium/F12 medium (Invitrogen/Life Technologies) and adding with 1% penicillin/streptomycin (Life Technologies), 2 mM L-glutamine (Life Technologies), 1:100 B27 supplement without vitamin A (Life Technologies) and 1:200 N2 supplement (Life Technologies). Maintenance medium was made of high-glucose N2B27 medium supplemented with 150 μM ascorbic acid (Sigma Aldrich), 0.5 μM PMA (Enzo Life Sciences) and 3 μM CHIR (Axon Medchem). Differentiation medium was made of high-glucose N2B27 medium supplemented with 200

μM ascorbic acid, 0.01 ng/μL BDNF (PeproTech), 0.01 ng/μL GDNF (PeproTech), 0.001 ng/μL TGFβ-3 (PeproTech), 2.5 μM dbcAMP (Sigma-Aldrich), and 1 μM PMA (absent after 6 days of differentiation).

^{13}C labeled maintenance medium and differentiation medium were made by replacing 20.4 mM glucose with the same amount of D-$^{13}C_6$-glucose so that the pool size of glucose remains the same. ^{15}N labeled maintenance medium and differentiation medium were made by replacing 2 mM glutamine with the same amount of L-$^{15}N_2$-glutamine so that the pool size of glutamine remains the same.

3. Cell culture

For method development and evaluation, the iPSCs-derived human neuroepithelial stem cells (hNESCs) were cultured on a 12-well plate at a density of 300,000 cells/well. Five wells of hNESCs were incubated with maintenance medium containing D-$^{13}C_6$-glucose, and another five wells of hNESCs were incubated with maintenance medium containing L-$^{15}N_2$-glutamine. Two wells of hNESCs were incubated with normal maintenance medium. The incubation time was 24 h. The ^{13}C and ^{15}N-labeled cellular samples were used as labeled reference samples for method evaluation.

Next, for method application, hNESCs were cultured and differentiated into mid-brain neurons on a 12-well plate at a density of 180,000 cells/well by following the established protocol.[33,34] After 21 days of neuron differentiation and maturation, we switched the normal differentiation medium into ^{13}C or ^{15}N-labeled differentiation medium. In the ^{13}C-labeling culture with D-$^{13}C_6$-glucose ($^{13}C_6$-Gluc), five replicates of labeled neuron culture were designed for the healthy group and the rotenone (200 nM) exposure group, respectively, and were accompanied by one unlabeled neuron culture within each group. The same sample design was applied in the ^{15}N labeling culture with L-$^{15}N_2$-glutamine ($^{15}N_2$-Gln). Differentiated neurons were under incubation with tracers for 24 h and reached isotopic labelling stationarity in metabolites. For cell quenching, ice cold 200 μL of 80% MeOH was added immediately after removing the spent medium and washing with phosphate buffered saline (Gibco/Life Technologies). The quenched cell samples were harvested into a new Eppendorf tube. Cellular samples were fast frozen into liquid nitrogen and stored in the -80 ℃ freezer until LC-MS measurement. Results from unlabeled neurons were used for qualitative peak confirmation during data analysis.

4. Sample preparation

Cell samples were lysed with sonication after one freeze-thaw cycle, vortexed and then centrifuged at 16000 g 4 ℃ for 10 min. Cell pellets were collected to measure the protein content using a bicinchoninic acid assay (Thermo Fisher Scientific Inc, United State). Supernatants were transferred into clean 1.5 mL Eppendorf tubes and evaporated to dryness

in a Labcono SpeedVac (MO, United State). Each sample was reconstituted with 60 µL ice-cold methanol/water (80%/20%; v/v). 50 µL of the reconstitution volume was collected and transferred into a new Eppendorf tube. The leftover volume was pooled together as a quality control (QC) sample for each group. Next the reconstituted samples and QC samples were processed with liquid-liquid extraction by adding 40 µL of ice-cold methanol/water (80%/20%; v/v), 45 µL of ice-cold Milli-Q water, and 65 µL of ice-cold chloroform, then followed with mixing and vortexing for 5 min and centrifuging at 16000 g 4 ℃ for 10 min. 130 µL of the aqueous phase was transferred into a new Eppendorf tube and extracted again by adding 25 µL of ice-cold methanol/water (50%/50%; v/v) and 65 µL of ice-cold chloroform, then followed with mixing and vortexing for 5 min and centrifuging at 16000 rcf, 4 ℃ for 10 min. Finally, 140 µL of the aqueous phase was transferred and taken to dryness. The residue was reconstituted with 50 µL of ice-cold methanol/water (50%/50%; v/v) as the final injection solution for LC-MS measurement. A series of diluted reference samples was prepared by diluting the ^{13}C-labeled reference sample twofold (DF_2x) and threefold (DF_3x) with the injection solvent of methanol/water (50%/50%; v/v).

5. LC-MS measurement

Chromatographic separation was performed using the SeQuant ZIC-c HILIC HPLC column (2.1mm x 100 mm, 3.0 µm, Merck, Darmstadt, Germany) on a Shimadzu Nexera Ultra high-performance liquid chromatograph (LC) (Duisburg, Germany). The LC method was adapted from a previously described method.[35] Mobile phase A consists of 90% acetonitrile, 10% water with 5 mM ammonium formate, and mobile phase B consists of 10% acetonitrile, 90% water with 5 mM ammonium formate. The injection volume was 3 µL. The flow rate was 0.5 mL/min and the gradient was as follows: 0 min-0% B, 2 min-15% B, 5 min-21% B, 7.5 min-26% B, from 10 to 11 min-40% B, from 11.5 to 18 min-0% B. The MS analyses were performed on a SCIEX ZenoTOF 7600 system (Darmstadt, Germany) with TwinSpray Turbo V ion source and operated in negative electrospray ionization. The following ion source parameters were applied: a spray voltage of 4.5 kV, a capillary temperature of 400 °C, ion source gas 1 of 20 psi, ion source gas 2 of 50 psi, curtain gas of 25 psi, CAD gas of 7 psi.

A SWATH acquisition method was able to fragment all isotopologues within stacked mass windows over the chromatographic run. Each MS cycle starts with a survey TOF MS scan in 100 ms from 50 to 700 Da using declustering potential (DP) at -80 eV and collision energy (CE) at -5 eV, followed by a fixed Q1 isolation window setting. The Q1 isolation strategy covered a mass range of *m/z* 60-690 with a 40 Da window width for Q1 isolation (overlap 1 Da). It allowed all possible isotopologues of each target metabolite to be fragmented in the same window. The SWATH scan accumulation time was 85 ms and each

cycle time was 1.576 s, using DP at -80 eV and CE at -30 eV±20 eV. We also tested additional SWATH window settings where the targeted isotopologues fell in two adjacent windows. The curated window settings can be seen in the supporting information, Table S2 and Figure S1.

The MRM^{HR} acquisition method consisted of the same TOF MS scan applied in the SWATH acquisition method, followed by MS/MS scans of the inclusion precursors with unit Q1 isolation and scheduled retention times. The targeted precursors are different for ^{13}C and ^{15}N-labeled sample analysis. Based on the measurement of ^{13}C and ^{15}N-labeled reference cell samples, in total, 180 precursor ions from 25 metabolites were targeted in the ^{13}C-labeling MRM^{HR} acquisition method, and 55 precursor ions from 15 metabolites were targeted in the ^{15}N-labeling MRM^{HR} acquisition method (Table S3-4). DP at -80 eV and CE at -30 eV±20 eV were applied to all precursor ions to have a fair comparison to SWATH acquisition. The Zeno MRM^{HR} acquisition method was designed based on the MRM^{HR} acquisition method and set with the Zeno-trap on-demand above the collision-induced dissociation intensity threshold of 2000 cps.

6. Data analysis

Qualitative data analysis was performed using the SCIEX OS Explorer processing tool. The fragmentation behavior analysis used the online database Metlin[36] and mzCloud (https://www.mzcloud.org/) as references and was confirmed with our in-house MS^2 database using analytical standards (see supporting information). Quantitative data analysis was performed using the SCIEX OS Analytics processing tool. The peak areas of metabolite isotopologues in the MS^1 and MS^2 levels were integrated and further corrected for the natural stable isotope abundance using software IsoCor.[37] MID represent the relative abundance of different mass isotopologues and are reported as isotopologue fractions. The ^{13}C/^{15}N enrichment refers to the mean content of isotopic tracer in the metabolite. It was calculated by the formula $\mathrm{ME} = (\sum_{i=1}^{n} \mathrm{Mi} * \mathrm{i})/\mathrm{n}$, where Mi is the proportion of isotopologues with i ^{13}C atoms for a metabolite containing n carbon atoms. Tandem MID analysis was calculated based on the primary MID and further applied with the secondary distribution ratio of isotopomers.

Results and discussion

To meet the study goal of capturing both intact and fragment-labeled isotopologue distributions of metabolites, we developed a MS/MS quantification method based on Zeno MRM^{HR} acquisition coupled to a HILIC separation method. Given the fact that a high number of transitions results in fewer scan points for each transition in the same retention time window, we first optimized the mobile phase gradient of a previously developed HPLC method utilizing a ZIC-c HILIC column for polar metabolite analysis.

1. HILIC-Zeno MRM^{HR} method development

In total, 40 polar metabolites derived from primary carbon metabolism, glutathione metabolism, and purine and pyrimidine metabolism achieved good chromatographic separation for standard solutions (Table S1, Figure S2). For the HILIC-Zeno MRM^{HR} method, 25 selected metabolites including all possible isotopic states were included in the ^{13}C-labeling MS^2 fragmentation method, and 15 metabolites including all possible isotopic states were included in the ^{15}N-labeling MS^2 fragmentation method. The selected metabolites were critical intermediates in their relevant metabolic pathway and were detected in labeled states with a TOF MS scan in the reference ^{13}C (^{15}N) cellular sample set. Finally, for metabolites eluting at retention times between 4 and 6 min, where the peak density is the highest, the method ensured a minimum of eight scan points across chromatographic peaks at the base (Figure S3). Under both MS^1 and MS^2 levels, the method exhibited good linearity for targeted metabolites, with correlation coefficients mostly above 0.99 (Table S5).

With proper isolation window settings, SWATH methods have been reported for MID quantification of targeted metabolites and their fragments with good sensitivity and small error.[26] To confirm the impact of entire or partial isotopologue coverage in one Q1 window, as well as the impact of overlapping windows offering partial isotopologue coverage, several SWATH acquisition methods with various mass window settings were evaluated. Our results showed that the quantification of isotopologues that span two windows suffers from peak intensity loss and reduced fidelity (Figure S1). As a reference method for our subsequent method comparisons, we selected a SWATH method with a fixed Q1 isolation window to encompass the intact MID of target metabolites.

2. Evaluation of sensitivity and isotope fidelity

Next, we evaluated the HILIC-Zeno MRM^{HR} method on the quantification performance for precursor and fragment isotopologues and compared these to the HILIC-MRM^{HR} and HILIC-SWATH methods. As shown in **Figure 1**, in the MS^1 TOF level, minor differences in the peak area were detected because of the slight differences in MS scan cycle duration between SWATH, Zeno MRM^{HR} and MRM^{HR} methods. Whereas in the MS^2 level, a significant signal improvement with the Zeno MRM^{HR} method was observed for all fragment and residual precursor isotopologues in comparison to SWATH and MRM^{HR} methods. The Zeno trap enables almost 100% duty cycle in MS/MS, resulting in signal gains without loss of mass accuracy or resolution.[38] The Zeno trap method improved the signal for fragment ions more than for their precursor ion, mostly because of a higher Zeno pulsing gain for lower masses. In comparison to SWATH, the ^{13}C-glutamate precursor increased 4.9-fold, while its fragment increased 7.8-fold; the ^{13}C-glutathione precursor

increased 4.7-fold, and its fragment increased 7.9-fold with the Zeno trap enabled. Significant sensitivity increases were also seen using the test results for ^{15}N-labeled reference cell samples (Figure S4). Precursor ions of ^{15}N-glutamate showed an increase of 6.6-fold, and fragment ions of ^{15}N-glutamate showed an increase of 8.4-fold compared to the SWATH method.

Moreover, the sensitivity gain still maintains an accurate MID. For metabolites containing 5 carbons (glutamate), or 10 carbons (glutathione), shown in **Figure 2**, the SWATH, Zeno MRM^{HR} and MRM^{HR} methods shared the same TOF MID results; in addition, the precursor MID was in line with the TOF MID. This provided confidence for further investigation of fragment MID. At the MS^2 fragment level, the Zeno MRM^{HR} method preserved identical ^{13}C isotopologue distributions as the other methods. No artefacts were introduced during Zeno trap pulsing in the Zeno trap. Likewise, for metabolites with one nitrogen (glutamate) or three nitrogens (glutathione) at both MS^1 and MS^2 levels, the Zeno MRM^{HR} results maintained identical ^{15}N isotopologue distribution as the other two methods (Figure S5). Overall, the HILIC-Zeno MRM^{HR} demonstrated its strong advantages in labeled mass isotopologue analysis in terms of detection sensitivity and isotope fidelity at the MS^2 level.

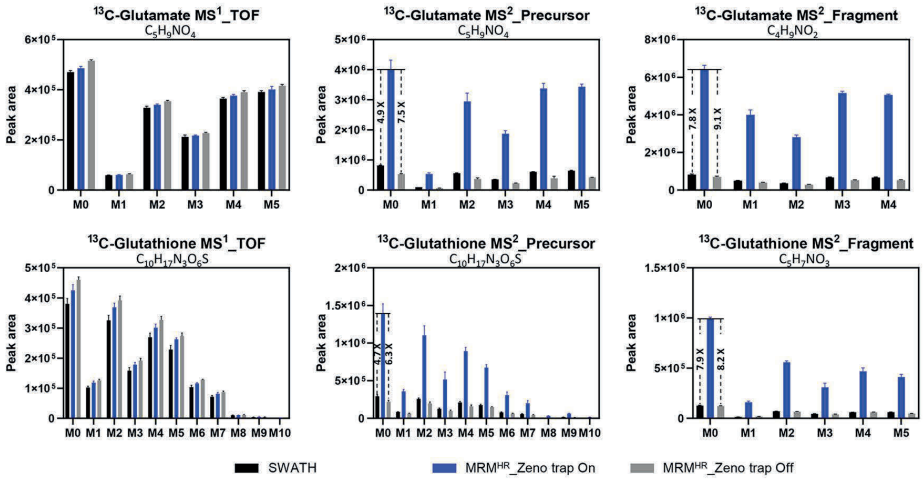

Figure 1. Sensitivity comparison at MS^1 TOF level and MS^2 fragmentation level among SWATH, MRM^{HR} and Zeno MRM^{HR} acquisition for ^{13}C labeled isotopologue analysis (n=3). At the MS^2 level, each precursor isotopologue was quantified using the peak area of residual precursor ion extracted from its MS/MS scan window. Each fragment isotopologue was quantified by summing the peak areas of the same fragment ion extracted from multiple MS/MS scan windows.

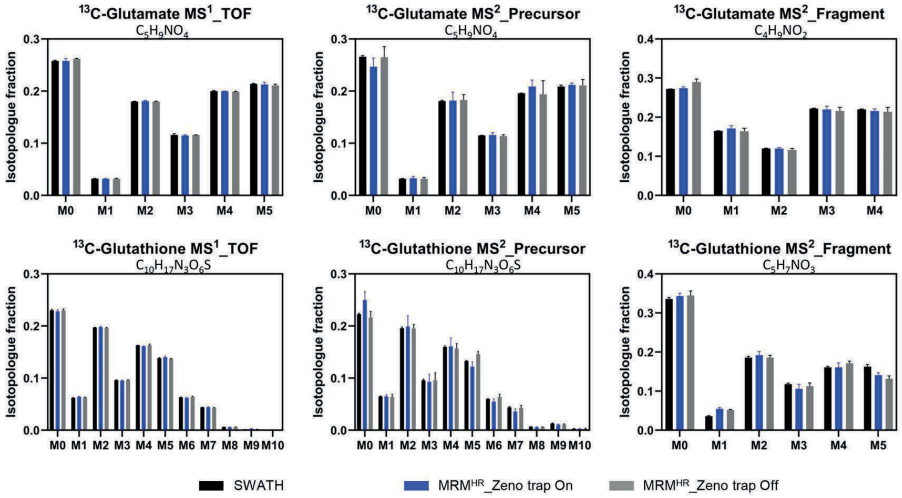

Figure 2. Accuracy comparison at MS^1 TOF level and MS^2 fragmentation level among SWATH, MRM^{HR} and Zeno MRM^{HR} acquisition for ^{13}C labeled isotopologue distribution analysis (n=3).

3. Evaluation of MID quantification reproducibility

In a typical cell culture, the harvested quantity of cells often varies between replicated culture wells. Nonetheless, regardless of variations in total cellular content, isotopologues in fractions should be constant among replicates of a group assuming a consistent metabolic state. We further evaluated the HILIC-Zeno MRM^{HR} method reproducibility in MID quantification for inter-sample analysis. A set of ^{13}C reference samples in undiluted form (DF_1x), twofold-dilution (DF_2x) and threefold dilution (DF_3x) was evaluated to imitate the effect of varied metabolite concentrations across samples. The average protein content corresponding to DF_1x, DF_2x and DF_3x samples was 38.0 µg, 19.0 µg and 12.7 µg respectively. As shown in Figure 3, for the metabolites glutamate, ketoglutarate, and glutathione, precursor MIDs had relative standard deviations (RSDs) between 6.7%-21.2%, and fragment MIDs had RSDs between 2.8%-10.1% across DF_1x, DF_2x and DF_3x samples. Fragment MID exhibited better quantification reproducibility than precursor MID. The corresponding MID data in detail can be found in Table S6. Overall, the MID quantification of the HILIC-Zeno MRM^{HR} method over inter-sample analysis demonstrated a reproducibility RSD of less than 25%. The performance of MS/MS fragmentation with the Zeno trap enabled showed good robustness to varied sample concentrations.

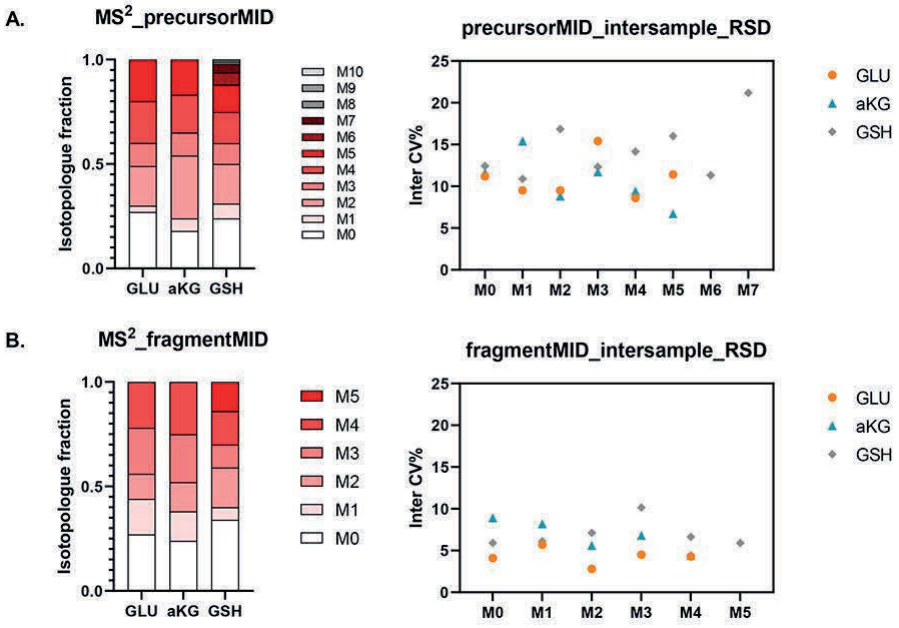

Figure 3. Inter-sample reproducibility of ^{13}C MIDs based on one reference sample set, including no dilution, twofold dilution, and threefold dilution. Each sample was injected three times. (A) Isotopologue fractions for precursor ions on average (left, n=9) and their corresponding RSD (right, n=9). (B) Isotopologue fractions for fragment ions on average (left, n=9) and their corresponding RSD (right, n=9). Glutamate: GLU; ketoglutarate: aKG; glutathione: GSH.

4. Tandem mass isotopologue distribution analysis of glutamate

One unique advantage of the HILIC-Zeno MRM^{HR} method is its capacity to resolve the labeling positional information for a particular isotopologue. To exemplify this, we used this method to distinguish two sets of ^{13}C labeling positions in the $^{13}C_2$-glutamate isotopologue derived from D-$^{13}C_6$-glucose. Figure 4A shows the detected M+0 precursor ion of glutamate and its produced fragments labeled in black, and the M+2 precursor ion and its produced fragments labeled in blue. Fragment_2 produced from M+2 isotopologue showed no labeled m+2 peak, indicating that simultaneous labeling of two ^{13}C atoms at the C4 and C5 positions was impossible. As illustrated in Figure 4B, glutamate derived from $^{13}C_6$-glucose after one round of ^{13}C incorporation via the tricarboxylic acid (TCA) cycle can result in two ^{13}C atoms at the C1 and C2 positions via pyruvate anaplerosis (PDH) and two ^{13}C atoms at the C3 and C4 positions via pyruvate carboxylase (PC) pathway.[39,40] By analyzing the corrected peak area ratio between the m+1 and m+2 peaks of fragment_1, we

could further determine the distribution ratio between 1,2-$^{13}C_2$-glutamate and 3,4-$^{13}C_2$-glutamate and generate a tandem MID of ^{13}C-glutamate in Figure 4C (Table S7). Healthy mid-brain neurons exhibited a relatively higher flux via PDH activity than PC activity.

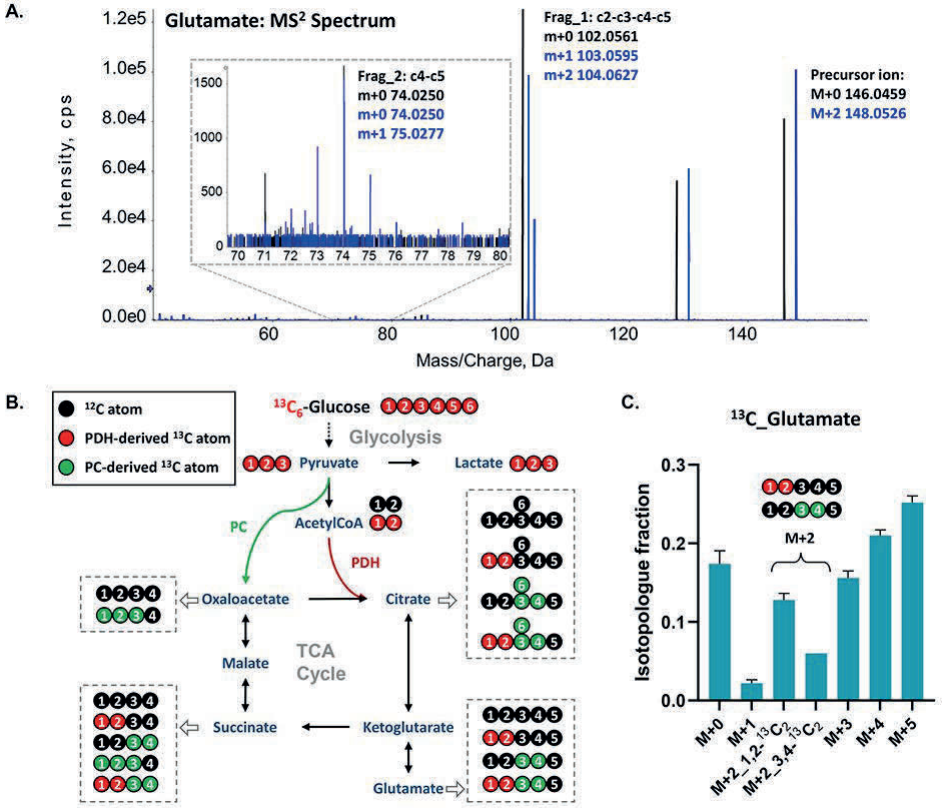

Figure 4. Structural elucidation of $^{13}C_2$-glutamate through analyzing the labeling pattern of annotated moiety fragment_1 (Frag_1: c2-c3-c4-c5) and fragment_2 (Frag_2: c4-c5) at the MS^2 level. (A) MS^2 spectrum of monoisotopic and $^{13}C_2$ isotopologue peak of ^{13}C-glutamate. (B) ^{13}C atom tracking derived from D-$^{13}C_6$-Glucose into glycolysis and the TCA cycle. The expected ^{13}C labeling patterns for the intermediates, acetylCoA, citrate, glutamate, succinate and oxaloacetate, via PDH and PC pathways were deduced and depicted in red and green, respectively. The first turn of PDH-initiated and PC-initiated ^{13}C labeling results were displayed. (C) Tandem MID of ^{13}C-glutamate measured in healthy neurons.

5. Reconstruction of glutathione metabolism in mid-brain neurons

Glutathione (GSH), one of the intracellular antioxidants, can protect cells by neutralizing reactive oxygen species and converting itself into its oxidized form (GSSG).[41] In modulating redox homeostasis, de novo GSH synthesis was reported to play a more critical

role than recycling GSSG.[42,43] Rotenone is known as a classic toxin for causing dopaminergic degeneration by inducing oxidative stress. To better distinguish the metabolic change of glutathione metabolism via de novo synthesis among intersecting pathways, the HILIC-Zeno MRM^{HR} method was applied to measure the polar $^{13}C/^{15}N$-metabolome from healthy and rotenone-treated mid-brain neurons with D-$^{13}C_6$-glucose/L-$^{15}N_2$-glutamine as a tracer.

The analyzed intact isotopologues of key intermediate metabolites from healthy neurons were first used to decipher the key pathway connection associated with de novo glutathione synthesis. In Figure 5A, for healthy mid-brain neurons, intermediates of ketoglutarate and glutamate, and serine and glycine were detected at 62 and 60%, and 11 and 7% levels of ^{13}C enrichment, respectively. GSH, GSSG showed 21 and 20% of ^{13}C enrichment originating from D-$^{13}C_6$-glucose, respectively. The incorporation of ^{13}C atoms from D-$^{13}C_6$-glucose into ketoglutarate and glutamate could be derived from the TCA cycle, and the ^{13}C incorporation into serine and glycine could be derived from the de novo serine synthetic branch of glycolysis. The deciphered pathway reconstruction based on the ^{13}C-enrichment of intermediates is shown in Figure 5B. Similarly, Figure 5C-D describes the pathway via ^{15}N atom flow into de novo GSH synthesis. By tracing the ^{15}N atoms from L-$^{15}N_2$-glutamine, 23 and 5% of ^{15}N enrichment were found in glutamate and serine, while no ^{15}N enrichment was detected in glycine. GSH, GSSG ultimately showed 5 and 4% of ^{15}N enrichment originated from L-$^{15}N_2$-glutamine, respectively. To be noted, neither ^{13}C nor ^{15}N labeling was found in cysteine, which suggested its independent supply from glucose or glutamine and instead a possible dependence on the essential uptake from the extracellular environment.

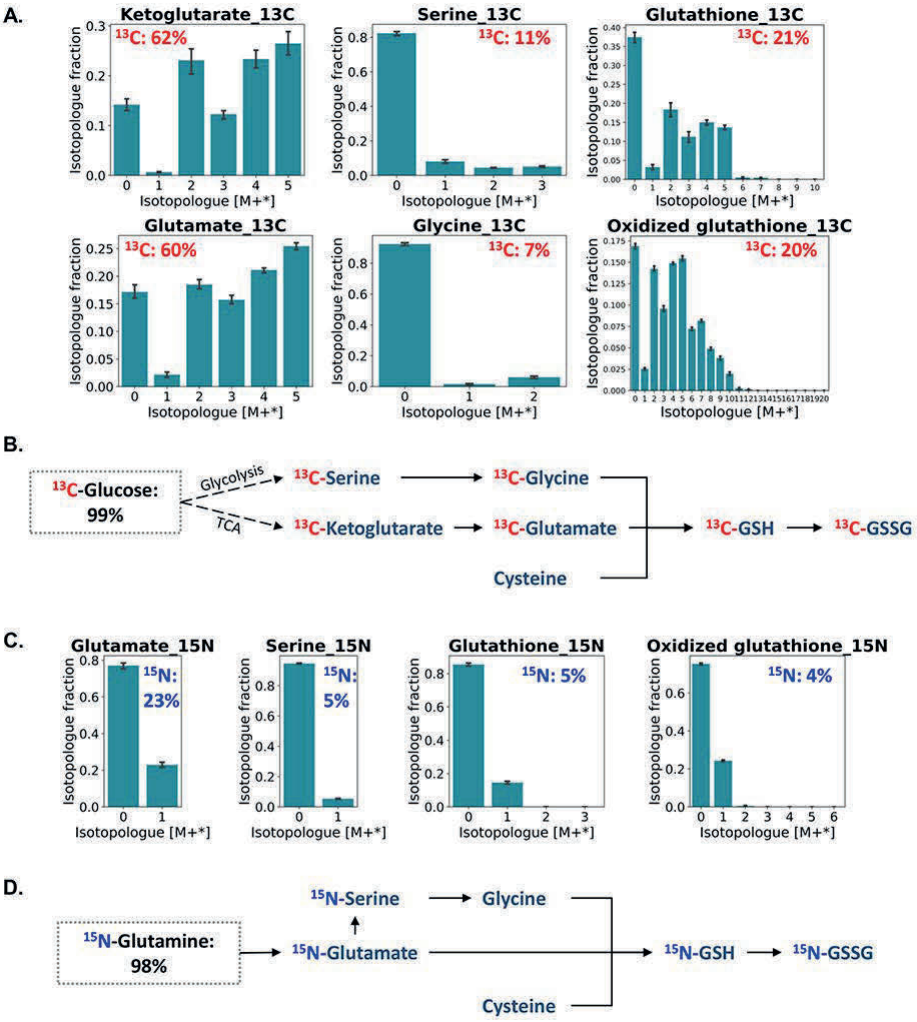

Figure 5. Tracing the de-novo glutathione synthesis pathway via $^{13}C/^{15}N$ atom enrichments of intermediate metabolites. The proportion of $^{13}C/^{15}N$ enrichment was denoted in red or blue. (A) ^{13}C labeled isotopologue distribution of intact metabolites. (B) ^{13}C atom flow in the de-novo glutathione synthesis pathway using D-$^{13}C_6$-glucose as a carbon tracer. (C) ^{15}N labeled isotopologue distribution of intact metabolites. (D) ^{15}N atom flow in the de-novo glutathione synthesis pathway using L-$^{15}N_2$-glutamine as a nitrogen tracer.

Based on the intact isotopologues of ^{13}C-GSH in M+1-7, we further investigated its fragment isotopologues (Figure 6), F1, indicating a glutamate moiety, was detected with a labeled distribution from m+0 to m+5 with 39% ^{13}C enrichment, which is similar to the

observed precursor glutamate MID pattern. In addition, F2, indicating a glycine-cysteine moiety, was detected with a labeled distribution from m+0 to m+2 and a ^{13}C enrichment of just 4%. This was consistent with the corresponding patterns of the precursors glycine and cysteine. ^{15}N-GSH was shown in M+1 via the intact isotopologue analysis. The ^{15}N enrichment is further observed only in the glutamate moiety (^{15}N-GSH F1) with its MID shown from m+0 to m+1. This moiety labeling pattern also matched the precursor glutamate MID. Besides the fact that the precursor serine was detected with certain ^{15}N enrichment, the level of ^{15}N-glycine and its incorporation as ^{15}N-GSH F2 could be too low to be detected. The fragment isotopologue distribution further validated the utilization of amino acid moieties derived from D-$^{13}C_6$-glucose/L-$^{15}N_2$-glutamine in the reconstructed pathway from Figure 5. Therefore, with the help of intact and fragment isotopologue analysis, we confirmed and highlighted the de novo synthesis of GSH in mid-brain neurons requires both glucose and glutamine for providing de novo-synthesized glutamate, serine, or glycine.

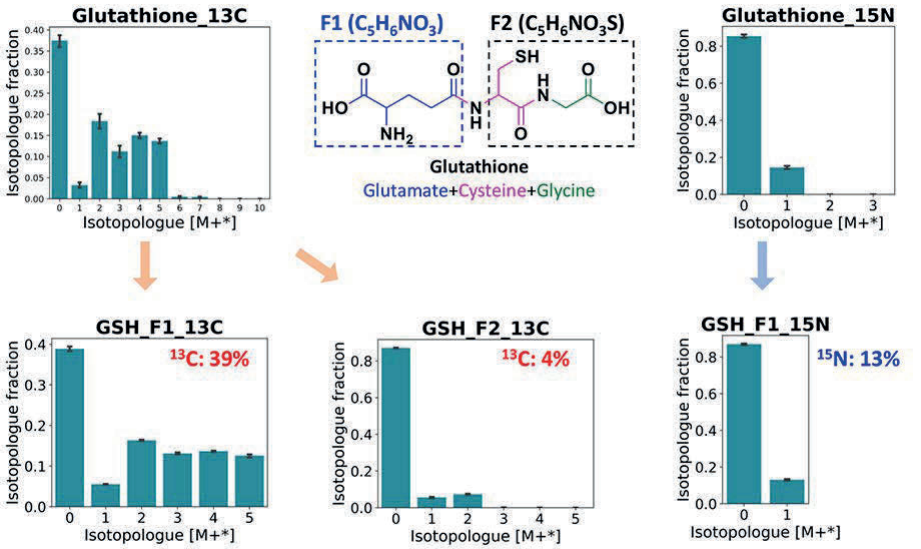

Figure 6. Structural elucidation of $^{13}C/^{15}N$-labeled glutathione via fragment isotopologue analysis. Ionized glutathione could produce a mass spectrum of fragments by collision-induced dissociation, from which fragment 1 (F1) indicated a glutamate moiety, fragment 2 (F2) indicated a glycine-cysteine moiety.

Rotenone inhibits mitochondrial complex I, impairing oxidative phosphorylation and resulting in a dramatic reduction of ATP production. It also produces excess generation of reactive oxygen species and leads to decreased GSH levels.[44] For mid-brain neurons with

rotenone treatment, we detected decreased ^{12}C-GSH and increased ^{12}C-GSSG compared to controls (Figure 7A). Apart from the ^{12}C-GSH pool, ^{13}C-GSH and ^{13}C-GSSG are synthesized de novo and both showed down-regulation. However, either the peak area ratio of ^{12}C-GSH/^{12}C-GSSG or the ratio of ^{13}C-GSH/^{13}C-GSSG was significantly decreased below 10 due to rotenone-induced oxidative stress (Figure 7B), which is consistent with a previous report.[45] Reduced peak area ratios of ^{14}N-GSH/^{14}N-GSSG and ratios of ^{15}N-GSH/^{15}N-GSSG were also found in ^{15}N labeled neurons (Figure 7D-E). A low GSH/GSSG ratio, as a result of antioxidant defense, may act as a critical factor in the neuroinflammatory and neurodegenerative processes in Parkinson's disease.[46] Interestingly, rotenone treatment also resulted in a significantly decreased labeled (^{13}C/^{15}N) fraction of the combined GSH+GSSG (Figure 7C and 7F), further implying defective GSH biosynthesis in rotenone-treated neurons.

To figure out the cause of low glutathione synthesis through de novo regulation, we next analyzed the ^{13}C/^{15}N-labeling patterns of both the intact molecule and its moieties for GSH and the associated intermediates (Figure 8). Rotenone induced significant depletion in both 1,2-$^{13}C_2$-glutamate and 3,4-$^{13}C_2$-glutamate, which pointed to inhibition of PDH and PC-mediated TCA cycle activity. Additionally, the ^{13}C-glutamate moiety of GSH (^{13}C-GSH F1) showed decreased ^{13}C fraction. This confirmed that rotenone reduced glutamate production by inhibiting the entry flux into upstream TCA cycle, rather than increasing its consumption for downstream synthesis. No significant depletion was observed in ^{13}C-glycine, while the ^{13}C-glycine moiety of GSH (^{13}C-GSH F2) showed a significantly decreased ^{13}C fraction after rotenone treatment. Based on the distribution ratio between m+0, m+1 and m+2 of F1 isotopologues (Table S8), a tandem analysis of ^{13}C-GSH including three positional isotopomers for M+2 isotopologue was obtained, as shown in Figure 8A. In line with the reduced ^{13}C enrichment found in GSH moieties F1 and F2, the abundance of two major isotopomers, $^{13}C_2$-GSH: M+2_Glu+$^{13}C_2$-Gly and M+2_$^{13}C_2$-Glu+Gly, decreased significantly in rotenone-treated conditions. Similar to the alterations of ^{13}C-glycine and ^{13}C-GSH F2, no change was found in ^{15}N-glutamate in the rotenone-treated group, while the ^{15}N-glutamate moiety of GSH (^{15}N-GSH F1) showed a significantly decreased ^{15}N fraction, and ^{15}N-GSH showed corresponding decreases in abundance (Figure 8B).

The results of mass isotopologue analysis showed that, in addition to suppressing glucose metabolism, which directly limits the source of glutamate supplied for de novo GSH synthesis, rotenone may also cause an inhibitory effect on the synthetic reaction of GSH production from glutamate, cysteine, and glycine. The sequential reactions are catalyzed by the ATP-dependent enzymes γ-glutamylcysteine synthetase (γ-GCS) and GSH synthetase (GS). Perceived flux reduction of reactions catalyzed by PDH, PC, γ-GCS and GS may be

a subsequent effect of mitochondrial complex I inhibition, which will need future validation to better understand the metabolic dysfunction during rotenone-induced neurodegeneration. Overall, our results suggest that in this neuronal model of rotenone-induced neurodegeneration, deficient de novo GSH synthesis and an increased oxidation into GSSG together resulted in a decreased GSH level under oxidative stress.

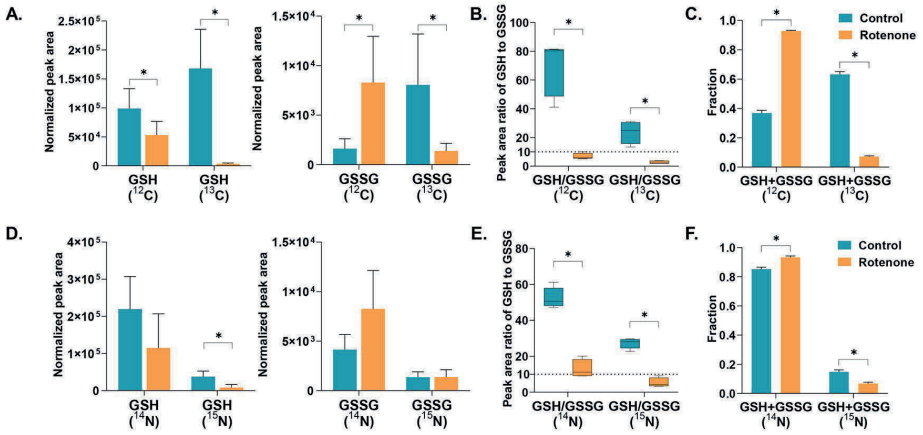

Figure 7. Metabolite abundance changes of glutathione (GSH) and oxidized glutathione (GSSG) under healthy and rotenone-treated conditions. (A) Bar plot representing the normalized peak area of ^{12}C/^{13}C GSH and GSSG. (B). Box plot representing the peak area ratio of ^{12}C-GSH to ^{12}C-GSSG and ^{13}C-GSH to ^{13}C-GSSG. (C) Bar plot representing the unlabeled (^{12}C) and labeled (^{13}C) fractions of combined GSH+GSSG. (D) Bar plot representing the normalized peak area of ^{14}N/^{15}N GSH and GSSG. (E) Box plot representing the peak area ratio of ^{14}N-GSH to ^{14}N-GSSG and ^{15}N-GSH to ^{15}N-GSSG. (F) Bar plot representing the unlabeled (^{14}N) and labeled (^{15}N) fractions of combined GSH+GSSG. Peak area was normalized using the corresponding sample protein content. An asterisk indicates a significant difference, with a p-value below 0.05.

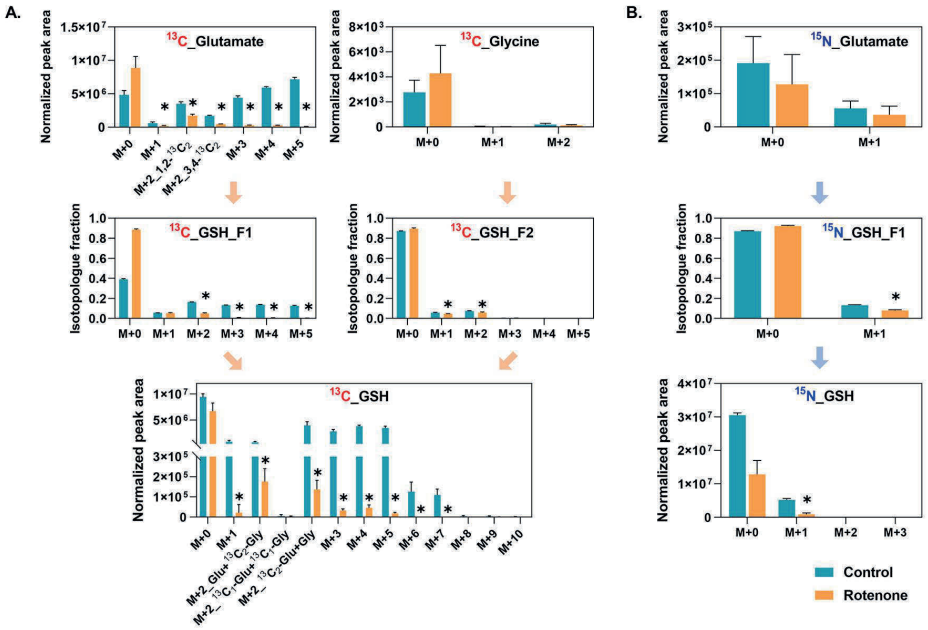

Figure 8. Mass isotopologue analysis of intact and fragmented metabolites for healthy and rotenone-perturbed mid-brain neurons. (A) ^{13}C labeled isotopologue analysis of glutamate, GSH and its moieties F1 and F2. The M+2 isotopologue of ^{13}C-glutamate was identified in two isotopomers. The M+2 isotopologue of ^{13}C-GSH was identified in three isotopomers. (B). ^{15}N-labeled isotopologue analysis of glutamate, GSH and its moiety F1. An asterisk indicates a significant difference, with a p-value below 0.05.

Conclusions

In this study, we developed a HILIC-Zeno MRM^{HR} method that can be used in tracer-based metabolomics studies for structurally-resolved MID analysis. This method allows the simultaneous acquisition at MS^1 and MS^2 levels in one single run. Labeled isotopologue distributions for intact metabolites can be obtained from the MS^1 level. Meanwhile, labeled isotopologue distributions for both the intact metabolite and its fragmented moieties can be obtained from the MS^2 level with higher sensitivity due to Zeno trap pulsing. The relationship between the labeled precursor and fragment ions was preserved to accurately identify the same labeled isotopologue with differential labeling positions. For future work, intensity-dependent selection of precursor ions can be combined with Zeno trap to trigger MS^2 for only present isotopologues, thus achieving even higher sensitivity. Furthermore, including additional target metabolites would provide more insight into pathway regulation, such as for γ-glutamylcysteine.

The method was successfully applied to analyze $^{13}C/^{15}N$-labeled polar extracts of human-derived mid-brain neurons under healthy and oxidatively stressed states using D-$^{13}C_6$-glucose/L-$^{15}N_2$-glutamine as tracers. By tracing the labeled $^{13}C/^{15}N$ atoms in the moieties of metabolite isotopologues, we were able to reconstruct the cell-type and condition-specific pathways of glutathione metabolism in healthy and perturbed mid-brain neurons. The quantitative isotopologue analysis greatly contributed to the new elucidation of glutathione metabolism regulation in response to rotenone perturbation. It is worth mentioning that quantitative isotopologue analysis highlights altered metabolic fluxes, providing guidance for the subsequent targeted analysis of changes in enzymatic activities, which expands our understanding of disease mechanisms at the enzyme level. Although we only present the application of our approach to glutathione metabolism, it can also be applied to study other pathways including central carbon metabolism and de novo nucleotide metabolism. Thereby, more accurate biological interpretations could be achieved within a cell-specific metabolic network.

Acknowledgments

This project received funding from the China scholarship coun-cil (No.201806210057), the European Union's Horizon 2020 research and innovation programme, for the SysMedPD project, under grant agreement No. 668738, the Dutch National Insti-tutes of Health (ZonMw) TKI-LSH Neuromet project (LSHM18092) and the Dutch Research Council (NWO) 'In-vestment Grant NWO Large' program, for the 'Building the infrastructure for Exposome research: Exposome-Scan' project (No. 175.2019.032). Additionally, we acknowledge Vincent Verschoor from Leiden University and Edinson Lucumi Moreno from Harvard University for their invaluable advice and assistance with neuron culture.

References

1. Grüning, N.-M.; Lehrach, H.; Ralser, M. Regulatory Crosstalk of the Metabolic Network. Trends in Biochemical Sciences 2010, 35 (4), 220–227.
2. Urbanczyk-Wochniak, E.; Luedemann, A.; Kopka, J.; Selbig, J.; Roessner-Tunali, U.; Willmitzer, L.; Fernie, A. R. Parallel Analysis of Transcript and Metabolic Profiles: A New Approach in Systems Biology. EMBO Rep 2003, 4 (10), 989–993.
3. Kell, D. B.; Brown, M.; Davey, H. M.; Dunn, W. B.; Spasic, I.; Oliver, S. G. Metabolic Footprinting and Systems Biology: The Medium Is the Message. Nat Rev Microbiol 2005, 3 (7), 557–565.
4. Shao, Y.; Le, W. Recent Advances and Perspectives of Metabolomics-Based Investigations in Parkinson's Disease. Molecular Neurodegeneration 2019, 14 (1), 3.
5. Anandhan, A.; Jacome, M. S.; Lei, S.; Hernandez-Franco, P.; Pappa, A.; Panayiotidis, M. I.; Powers, R.; Franco, R. Metabolic Disorder Dysfunction in Parkinson's Disease: Bioenergetics, Redox Homeostasis and Central Carbon Metabolism. Brain Res Bull 2017, 133, 12–30.
6. Watson, E.; Yilmaz, L. S.; Walhout, A. J. M. Understanding Metabolic Regulation at a Systems Level: Metabolite Sensing, Mathematical Predictions, and Model Organisms. Annu Rev Genet 2015, 49, 553–575.
7. Ma, W.; Trusina, A.; El-Samad, H.; Lim, W. A.; Tang, C. Defining Network Topologies That Can Achieve Biochemical Adaptation. Cell 2009, 138 (4), 760–773.
8. Truscott, R. J.; Malegan, D.; McCairns, E.; Halpern, B.; Hammond, J.; Cotton, R. G.; Mercer, J. F.; Hunt, S.; Rogers, J. G.; Danks, D. M. Two New Sulphur-Containing Amino Acids in Man. Biomed Mass Spectrom 1981, 8 (3), 99–104.

9. Yuan, M.; Kremer, D. M.; Huang, H.; Breitkopf, S. B.; Ben-Sahra, I.; Manning, B. D.; Lyssiotis, C. A.; Asara, J. M. Ex Vivo and in Vivo Stable Isotope Labelling of Central Carbon Metabolism and Related Pathways with Analysis by LC–MS/MS. Nat Protoc 2019, 14 (2), 313–330.
10. Ma, E. H.; Verway, M. J.; Johnson, R. M.; Roy, D. G.; Steadman, M.; Hayes, S.; Williams, K. S.; Sheldon, R. D.; Samborska, B.; Kosinski, P. A.; Kim, H.; Griss, T.; Faubert, B.; Condotta, S. A.; Krawczyk, C. M.; DeBerardinis, R. J.; Stewart, K. M.; Richer, M. J.; Chubukov, V.; Roddy, T. P.; Jones, R. G. Metabolic Profiling Using Stable Isotope Tracing Reveals Distinct Patterns of Glucose Utilization by Physiologically Activated CD8+ T Cells. Immunity 2019, 51 (5), 856-870.e5.
11. Berry, D.; Loy, A. Stable-Isotope Probing of Human and Animal Microbiome Function. Trends in Microbiology 2018, 26 (12), 999–1007.
12. Fernández-García, J.; Altea-Manzano, P.; Pranzini, E.; Fendt, S.-M. Stable Isotopes for Tracing Mammalian-Cell Metabolism In Vivo. Trends in Biochemical Sciences 2020, 45 (3), 185–201.
13. Peterson, A. L.; Walker, A. K.; Sloan, E. K.; Creek, D. J. Optimized Method for Untargeted Metabolomics Analysis of MDA-MB-231 Breast Cancer Cells. Metabolites 2016, 6 (4), 30.
14. Hui, S.; Ghergurovich, J. M.; Morscher, R. J.; Jang, C.; Teng, X.; Lu, W.; Esparza, L. A.; Reya, T.; Le Zhan; Yanxiang Guo, J.; White, E.; Rabinowitz, J. D. Glucose Feeds the TCA Cycle via Circulating Lactate. Nature 2017, 551 (7678), 115–118.
15. Creek, D. J.; Mazet, M.; Achcar, F.; Anderson, J.; Kim, D.-H.; Kamour, R.; Morand, P.; Millerioux, Y.; Biran, M.; Kerkhoven, E. J.; Chokkathukalam, A.; Weidt, S. K.; Burgess, K. E. V.; Breitling, R.; Watson, D. G.; Bringaud, F.; Barrett, M. P. Probing the Metabolic Network in Bloodstream-Form Trypanosoma Brucei Using Untargeted Metabolomics with Stable Isotope Labelled Glucose. PLOS Pathogens 2015, 11 (3), e1004689.
16. Creek, D. J.; Chokkathukalam, A.; Jankevics, A.; Burgess, K. E. V.; Breitling, R.; Barrett, M. P. Stable Isotope-Assisted Metabolomics for Network-Wide Metabolic Pathway Elucidation. Analytical Chemistry 2012, 84 (20), 8442–8447.
17. Feith, A.; Teleki, A.; Graf, M.; Favilli, L.; Takors, R. HILIC-Enabled 13C Metabolomics Strategies: Comparing Quantitative Precision and Spectral Accuracy of QTOF High- and QQQ Low-Resolution Mass Spectrometry. Metabolites 2019, 9 (4), 63.
18. Alves, T. C.; Pongratz, R. L.; Zhao, X.; Yarborough, O.; Sereda, S.; Shirihai, O.; Cline, G. W.; Mason, G.; Kibbey, R. G. Integrated, Step-Wise, Mass-Isotopomeric Flux Analysis of the TCA Cycle. Cell Metabolism 2015, 22 (5), 936–947.
19. Antoniewicz, M. R. Tandem Mass Spectrometry for Measuring Stable-Isotope Labeling. Current Opinion in Biotechnology 2013, 24 (1), 48–53.
20. Choi, J.; Antoniewicz, M. R. Tandem Mass Spectrometry: A Novel Approach for Metabolic Flux Analysis. Metabolic Engineering 2011, 13 (2), 225–233.
21. Yuan, J.; Bennett, B. D.; Rabinowitz, J. D. Kinetic Flux Profiling for Quantitation of Cellular Metabolic Fluxes. Nature Protocols 2008, 3 (8), 1328–1340.
22. Rühl, M.; Rupp, B.; Nöh, K.; Wiechert, W.; Sauer, U.; Zamboni, N. Collisional Fragmentation of Central Carbon Metabolites in LC-MS/MS Increases Precision of 13C Metabolic Flux Analysis. Biotechnol. Bioeng. 2012, 109 (3), 763–771.
23. McCloskey, D.; Young, J. D.; Xu, S.; Palsson, B. O.; Feist, A. M. MID Max: LC–MS/MS Method for Measuring the Precursor and Product Mass Isotopomer Distributions of Metabolic Intermediates and Cofactors for Metabolic Flux Analysis Applications. Anal. Chem. 2016, 88 (2), 1362–1370.
24. Mairinger, T.; Hann, S. Implementation of Data-Dependent Isotopologue Fragmentation in 13C-Based Metabolic Flux Analysis. Anal Bioanal Chem 2017, 409 (15), 3713–3718.
25. Gillet, L. C.; Navarro, P.; Tate, S.; Röst, H.; Selevsek, N.; Reiter, L.; Bonner, R.; Aebersold, R. Targeted Data Extraction of the MS/MS Spectra Generated by Data-Independent Acquisition: A New Concept for Consistent and Accurate Proteome Analysis. Mol Cell Proteomics 2012, 11 (6), O111.016717.
26. Jaiswal, D.; Prasannan, C. B.; Hendry, J. I.; Wangikar, P. P. SWATH Tandem Mass Spectrometry Workflow for Quantification of Mass Isotopologue Distribution of Intracellular Metabolites and Fragments Labeled with Isotopic 13 C Carbon. Analytical Chemistry 2018, 90 (11), 6486–6493.
27. Siegel, D.; Meinema, A. C.; Permentier, H.; Hopfgartner, G.; Bischoff, R. Integrated Quantification and Identification of Aldehydes and Ketones in Biological Samples. Anal. Chem. 2014, 86 (10), 5089–5100.
28. Sun, Q.; Fan, T. W.-M.; Lane, A. N.; Higashi, R. M. An Ion Chromatography–Ultrahigh-Resolution-MS 1 /Data-Independent High-Resolution MS 2 Method for Stable Isotope-Resolved Metabolomics Reconstruction of Central Metabolic Networks. Anal. Chem. 2021, 93 (5), 2749–2757.
29. Jaiswal, D.; Wangikar, P. P. SWATH: A Data-Independent Tandem Mass Spectrometry Method to Quantify 13C Enrichment in Cellular Metabolites and Fragments. In Metabolic Flux Analysis in Eukaryotic Cells: Methods and Protocols; Nagrath, D., Ed.; Methods in Molecular Biology; Springer US: New York, NY, 2020; pp 189–204.
30. Choi, J.; Antoniewicz, M. R. Tandem Mass Spectrometry: A Novel Approach for Metabolic Flux Analysis. Metabolic Engineering 2011, 13 (2), 225–233.
31. Mairinger, T.; Steiger, M.; Nocon, J.; Mattanovich, D.; Ko-ellensperger, G.; Hann, S. Gas Chromatography-Quadrupole Time-of-Flight Mass Spectrometry-Based Determination of Isotopologue and Tandem Mass Isotopomer Fractions of Primary Metabolites for 13 C-Metabolic Flux Analysis. Anal. Chem. 2015, 87 (23), 11792–11802.

32. Chernushevich, I. V.; Merenbloom, S. I.; Liu, S.; Bloomfield, N. A W-Geometry Ortho-TOF MS with High Resolution and Up to 100% Duty Cycle for MS/MS. J. Am. Soc. Mass Spectrom. 2017, 28 (10), 2143–2150.
33. Reinhardt, P.; Glatza, M.; Hemmer, K.; Tsytsyura, Y.; Thiel, C. S.; Höing, S.; Moritz, S.; Parga, J. A.; Wagner, L.; Bruder, J. M.; Wu, G.; Schmid, B.; Röpke, A.; Klingauf, J.; Schwamborn, J. C.; Gasser, T.; Schöler, H. R.; Sterneckert, J. Derivation and Expansion Using Only Small Molecules of Human Neural Progenitors for Neurodegenerative Disease Modeling. PLoS ONE 2013, 8 (3), e59252.
34. Moreno, E. L.; Hachi, S.; Hemmer, K.; Trietsch, S. J.; Baumuratov, A. S.; Hankemeier, T.; Vulto, P.; Schwamborn, J. C.; Fleming, R. M. T. Differentiation of Neuroepithelial Stem Cells into Functional Dopaminergic Neurons in 3D Microfluidic Cell Culture. Lab on a Chip 2015, 15 (11), 2419–2428.
35. Hosseinkhani, F.; Huang, L.; Dubbelman, A.-C.; Guled, F.; Harms, A. C.; Hankemeier, T. Systematic Evaluation of HILIC Stationary Phases for Global Metabolomics of Human Plasma. Metabolites 2022, 12 (2), 165.
36. Guijas, C.; Montenegro-Burke, J. R.; Domingo-Almenara, X.; Palermo, A.; Warth, B.; Hermann, G.; Koellensperger, G.; Huan, T.; Uritboonthai, W.; Aisporna, A. E.; Wolan, D. W.; Spilker, M. E.; Benton, H. P.; Siuzdak, G. METLIN: A Technology Platform for Identifying Knowns and Unknowns. Anal Chem 2018, 90 (5), 3156–3164.
37. Millard, P.; Delépine, B.; Guionnet, M.; Heuillet, M.; Bellvert, F.; Létisse, F. IsoCor: Isotope Correction for High-Resolution MS Labeling Experiments. Bioinformatics 2019, 35 (21), 4484–4487.
38. Loboda, A. V.; Chernushevich, I. V. A Novel Ion Trap That Enables High Duty Cycle and Wide m/z Range on an Orthogonal Injection TOF Mass Spectrometer. Journal of the American Society for Mass Spectrometry 2009, 20 (7), 1342–1348.
39. Yang, Y.; Fan, T. W.-M.; Lane, A. N.; Higashi, R. M. Chloroformate Derivatization for Tracing the Fate of Amino Acids in Cells and Tissues by Multiple Stable Isotope Resolved Metabolomics (MSIRM). Analytica chimica acta 2017, 976, 63—73.
40. Fan, T. W.-M.; Sun, Q.; Higashi, R. M. Ultrahigh Resolution MS1/MS2-Based Reconstruction of Metabolic Networks in Mammalian Cells Reveals Changes for Selenite and Arsenite Action. Journal of Biological Chemistry 2022, 298 (12), 102586.
41. Kurutas, E. B. The Importance of Antioxidants Which Play the Role in Cellular Response against Oxidative/Nitrosative Stress: Current State. Nutr J 2016, 15, 71.
42. Townsend, D. M.; Tew, K. D.; Tapiero, H. The Importance of Glutathione in Human Disease. Biomed Pharmacother 2003, 57 (3–4), 145–155.
43. Lian, G.; Gnanaprakasam, J. R.; Wang, T.; Wu, R.; Chen, X.; Liu, L.; Shen, Y.; Yang, M.; Yang, J.; Chen, Y.; Vasiliou, V.; Cassel, T. A.; Green, D. R.; Liu, Y.; Fan, T. W.; Wang, R. Glutathione de Novo Synthesis but Not Recycling Process Coordinates with Glutamine Catabolism to Control Redox Homeostasis and Directs Murine T Cell Differentiation. eLife 7, e36158.
44. Testa, C. M.; Sherer, T. B.; Greenamyre, J. T. Rotenone Induces Oxidative Stress and Dopaminergic Neuron Damage in Organotypic Substantia Nigra Cultures. Molecular Brain Research 2005, 134 (1), 109–118.
45. Wu, G.; Fang, Y.-Z.; Yang, S.; Lupton, J. R.; Turner, N. D. Glutathione Metabolism and Its Implications for Health. The Journal of Nutrition 2004, 134 (3), 489–492.
46. Bjørklund, G.; Peana, M.; Maes, M.; Dadar, M.; Severin, B. The Glutathione System in Parkinson's Disease and Its Progression. Neuroscience & Biobehavioral Reviews 2021, 120, 470–478.

Supplementary Materials

1. Optimal mass isolation window setting for SWATH acquisition method

When optimizing a SWATH acquisition method, considerations need to be made defining scan time, window size and total number of windows. Additional considerations need to be made in tracer-based studies especially when analyzing diverse metabolites. In this case, for accurate quantitation, all isotopologues of a certain metabolite need to be in the same Q1 window and care should be taken to prevent the underestimated integration of the mass isotopologue located on the edge of a SWATH window.[1] This experiment was designed to test the effect of complete or partial isotopologue coverage in one Q1 window, as well as the influence of overlapping windows giving partial isotopologue coverage. In total four SWATH methods were created with varied Q1 isolation windows and window overlap, as shown in Table S2. Each SWATH method starts with a survey TOF MS scan in 100 ms

from 50 to 700 Da, followed by sixteen Q1 isolation windows covering a mass range of *m/z* 60-690. The relevant Q1 isolation windows in each SWATH method targeting ^{13}C labeled glutamate were listed in Figure S1, also recorded in cycleID of 2 and 3 from Table S2. SWATH_Win1 and Win4 methods allow glutamate isotopologues of M0-M5 to be measured and quantified in the same window, but SWATH_Win2 and Win3 methods measured and quantified isotopologues across the two neighboring windows.

As a result, SWATH_Win1 and Win4 methods shared similar isotopologue quantification on both isotopologue peak area and isotopologue fraction which was also comparable to the results of general MRM^{HR} acquisition. However, the SWATH_Win2 method had lower signal for the M0-M2 isotopologues and this led to a change in their mass isotopologue fractions. The increased window overlapping width of 3.0 Da in the SWATH_Win3 method showed no improvement in isotopologue quantification combining neighboring windows. The results indicated a big drawback for the quantification of isotopologues of metabolites that span multiple windows, which would also cause subsequent inaccuracies in the quantification of fragment isotopologues. For targeted labeled metabolite analysis, it is strongly recommended to refine the Q1 window setting to include all possible isotopologues of precursor ions, even with the demand of making a custom SWATH window program or creating variable Q1 isolation windows.[1,2] In this study, the SWATH_Win1 method with fixed Q1 isolation window was finally selected for the formal comparison with general MRM^{HR}, and Zeno MRM^{HR} acquisition.

SWATH method	CycleID	Overlap window width	*m/z* begin	*m/z* end	Quantified mass isotopologue
SWATH_Win1	2	1.0 Da	99	140	\
	3		139	180	M0,M1,M2,M3,M4,M5
SWATH_Win2	2	1.0 Da	99	149	**M0,M1,M2**
	3		148	180	M3,M4,M5
SWATH_Win3	2	3.0 Da	97	149	**M0**
	3		146	180	M1,M2,M3,M4,M5
SWATH_Win4	2	5.0 Da	95	149	\
	3		144	180	M0,M1,M2,M3,M4,M5

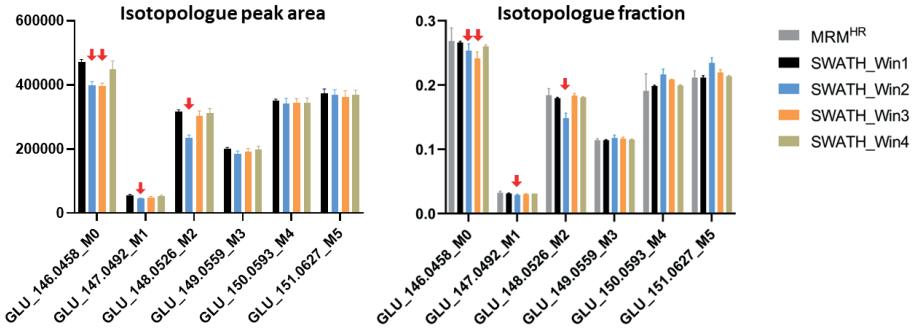

Figure S1. Peak integration influence on target metabolite isotopologues spanning across two neighboring SWATH mass isolation windows compared to complete isotopologues detection within a single window.

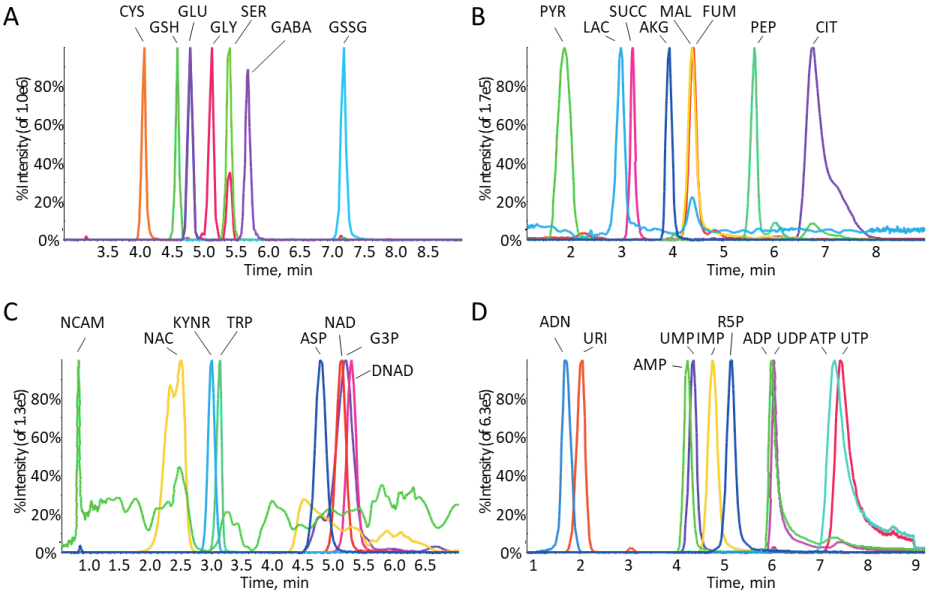

Figure S2. Extracted ion chromatography of target metabolites from de novo glutathione synthesis (A), primary carbon metabolism (B), de novo NAD synthesis (C), purine and pyrimidine metabolism (D). The metabolite abbreviations were introduced in Table S1.

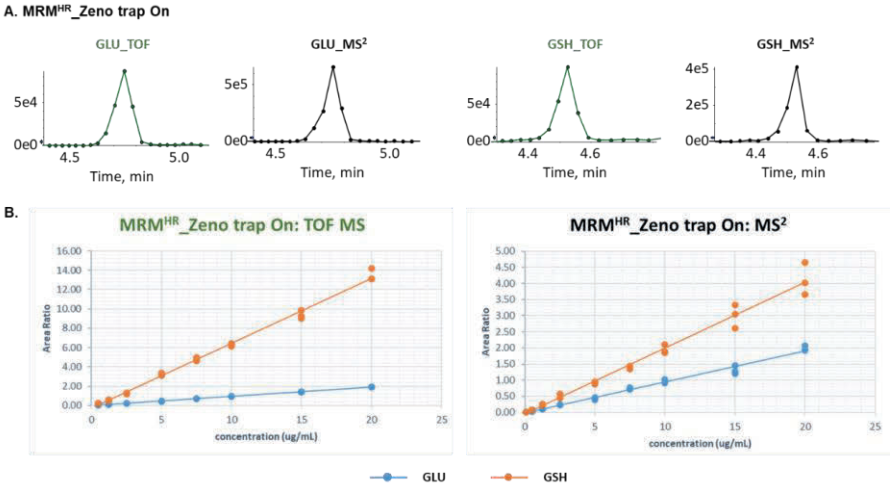

Figure S3. A. Illustration of peak scan points for metabolites glutamate (GLU) and glutathione (GSH) eluting between 4 and 6 mins, using ^{13}C labeling Zeno MRM^{HR} acquisition method; B. Linearity test of glutamate (GLU) and glutathione (GSH) based on the quantification for TOF-MS and MS/MS level.

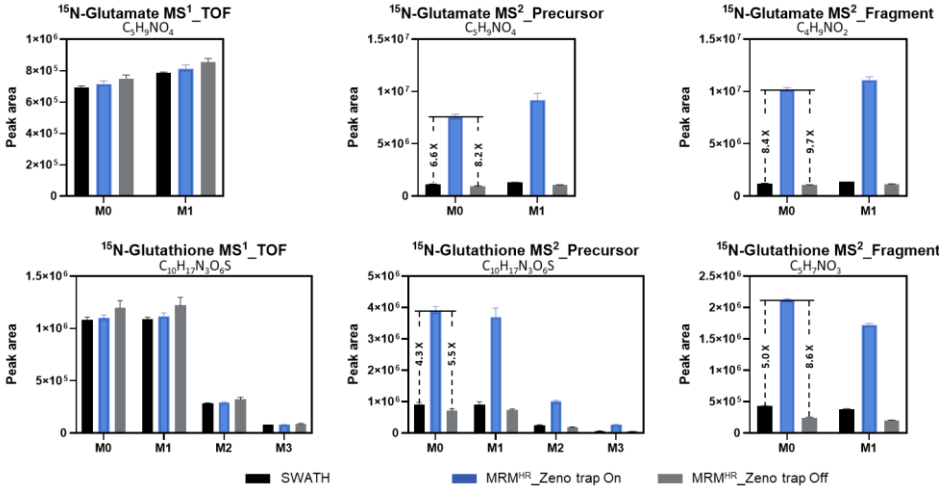

Figure S4. Sensitivity comparison at MS^1 TOF level and MS^2 fragmentation level among SWATH, MRM^{HR} and Zeno MRM^{HR} acquisition for ^{15}N labeled isotopologue analysis (n=3). At the MS^2 level, each precursor isotopologue was quantified using the peak area of residual precursor ion extracted from its MS/MS scan window. Each fragment isotopologue was quantified by summing the peak areas of the same fragment ion extracted from multiple MS/MS scan windows.

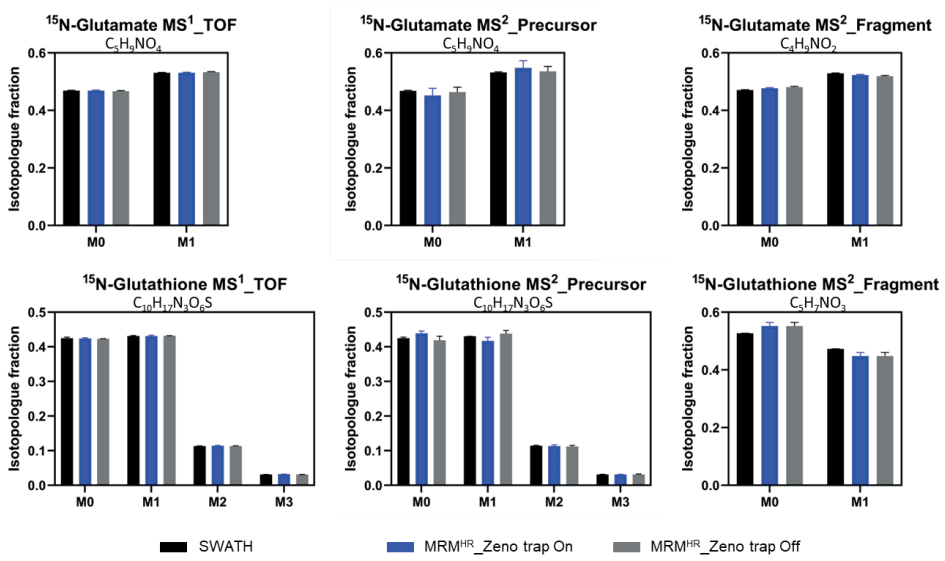

Figure S5. Accuracy comparison at MS^1 TOF level and MS^2 fragmentation level between SWATH, MRM^{HR} and Zeno MRM^{HR} acquisition for ^{15}N labeled isotopologue distribution analysis (n=3).

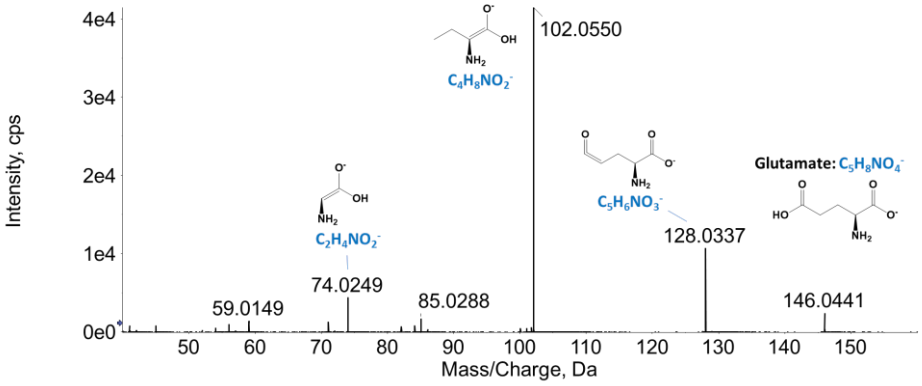

Figure S6. Product ion fragment annotation of glutamate.

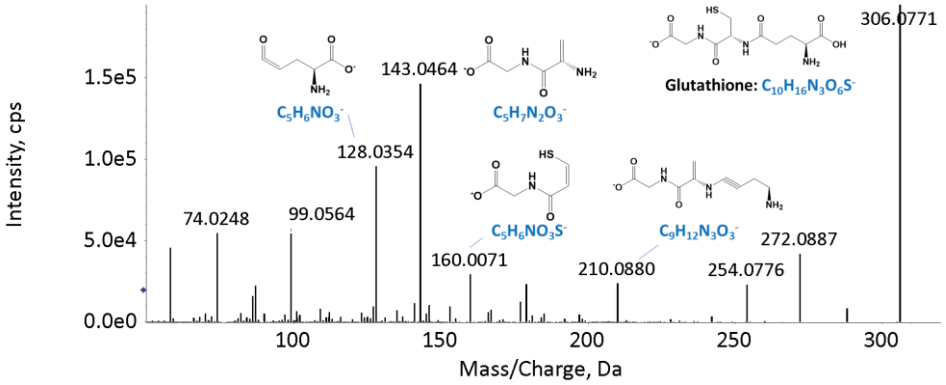

Figure S7. Product ion fragment annotation of glutathione.

References

47. Jaiswal, D.; Prasannan, C. B.; Hendry, J. I.; Wangikar, P. P. SWATH Tandem Mass Spectrometry Workflow for Quantification of Mass Isotopologue Distribution of Intracellular Metabolites and Fragments Labeled with Isotopic 13 C Carbon. Analytical Chemistry 2018, 90 (11), 6486–6493.

48. Zhang, Y.; Bilbao, A.; Bruderer, T.; Luban, J.; Strambio-De-Castillia, C.; Lisacek, F.; Hopfgartner, G.; Varesio, E. The Use of Variable Q1 Isolation Windows Improves Selectivity in LC–SWATH–MS Acquisition. J. Proteome Res. 2015, 14 (10), 4359–4371.

Table S1: Target metabolite list prepared in individual stock solution

CHEBI ID	Metabolite Name	Abbreviation	Compound Formula	Mono-isotopic Mass/Da	Solvent	Retention time /min
16015	L-Glutamic acid	GLU	C5H9NO4	147.0532	50%MeOH (0.5M NaOH)	4.8
16865	gamma-Aminobutyric acid	GABA	C4H9NO2	103.0633	50%MeOH	5.7
15428	Glycine	GLY	C2H5NO2	75.0320	50%MeOH (0.5M NaOH)	5.1
17561	Cysteine	CYS	C3H7NO2S	121.0197	50%MeOH	4.1
17115	Serine	SER	C3H7NO3	105.0426	50%MeOH	5.4
16856	Glutathione	GSH	C10H17N3O6S	307.0838	50%MeOH	4.6
17858	Oxidized glutathione	GSSG	C20H32N6O12S2	612.1520	50%MeOH	7.1
17053	L-Aspartic acid	ASP	C4H7NO4	133.0375	50%MeOH (0.5M NaOH)	4.8
29052	Glyceraldehyde 3-Phosphate	G3P	C3H7O6P	169.9980	50%MeOH	5.2
16675	Quinolinic acid	QULN	C7H5NO4	167.0219	50%MeOH (0.1M NaOH)	4.6
18304	Nicotinic acid adenine dinucleotide	DNAD	C21H27N6O15P2	665.1010	50%MeOH	5.2
15846	Nicotinamide adenine dinucleotide	NAD	C21H27N7O14P2	663.1091	50%MeOH	5.1
15940	Nicotinic acid	NAC	C6H5NO2	123.0320	50%MeOH	2.5
17154	Niacinamide	NCAM	C6H6N2O	122.0480	50%MeOH	0.9
16828	L-Tryptophan	TRP	C11H12N2O2	204.0899	50%MeOH	3.2
16946	L-Kynurenine	KYNR	C10H12N2O3	208.0848	50%MeOH	3
52742	D-Ribose 5-phosphate	R5P	C5H11O8P	230.0192	50%MeOH	5.1
16695	Uridine 5'-monophosphate	UMP	C9H13N2O9P	324.0359	50%MeOH	4.3
17659	Uridine 5'-diphosphate	UDP	C9H14N2O12P2	404.0022	50%MeOH	5.8
15713	Uridine triphosphate	UTP	C9H15N2O15P3	483.9685	50%MeOH	7.2
16704	Uridine	URI	C9H12N2O6	244.0695	50%MeOH	2
18050	L-Glutamine	GLN	C5H10N2O3	146.0691	50%MeOH	5
17202	Inosine monophosphate	IMP	C10H13N4O8P	348.0470	50%MeOH (0.5M NaOH)	4.7
17596	Inosine	INS	C10H12N4O5	268.0808	50%MeOH	2.9
16027	Adenosine monophosphate	AMP	C10H14N5O7P	347.0631	50%MeOH	4.2
16761	Adenosine diphosphate	ADP	C10H15N5O10P2	427.0294	50%MeOH	5.8
15422	Adenosine triphosphate	ATP	C10H16N5O13P3	506.9957	50%MeOH	7
16335	Adenosine	ADN	C10H13N5O4	267.0968	50%MeOH (12M 37% HCL)	1.7
17345	Guanosine monophosphate	GMP	C10H14N5O8P	363.0580	50%MeOH	5.3
17552	Guanosine diphosphate	GDP	C10H15N5O11P2	443.0243	50%MeOH	7.2
15996	Guanosine triphosphate	GTP	C10H16N5O14P3	522.9906	50%MeOH	8.3

16750	Guanosine	GSN	C10H13N5O5	283.0917	50%MeOH (12M 37% HCL)	3.3
30915	Oxoglutaric acid	AKG	C5H6O5	146.0215	50%MeOH	3.9
30769	Citric acid	CIT	C6H8O7	192.0270	50%MeOH	6.7
15741	Succinic acid	SUCC	C4H6O4	118.0266	50%MeOH	3.1
18012	Fumaric acid	FUM	C4H4O4	116.0110	50%MeOH	4.3
30797	L-Malic acid	MAL	C4H6O5	134.0215	MiliQ water	4.2
32816	Pyruvic acid	PYR	C3H4O3	88.0160	50%MeOH	1.8
44897	Phosphoenolpyruvic acid	PEP	C3H5O6P	167.9824	50%MeOH	5.5
422	L-Lactic acid	LAC	C3H6O3	90.0317	50%MeOH	2.9

Table S2: Q1 mass isolation window setting design for different SWATH MS acquisition methods

		SWATH_Win1		SWATH_Win2		SWATH_Win3		SWATH_Win4	
CycleID	**Type**	**m/z begin**	**m/z end**	**m/z begin**	**m/z end**	**m/z begin**	**m/z end**	**m/z begin**	**m/z end**
0	SCAN	50	700	50	700	50	700	50	700
1	SWATH	60	100	60	100	60	100	60	100
2	**SWATH**	**99**	**140**	**99**	**149**	**97**	**149**	**95**	**149**
3	**SWATH**	**139**	**180**	**148**	**180**	**146**	**180**	**144**	**180**
4	SWATH	179	220	179	233	177	233	175	233
5	SWATH	219	260	232	260	230	260	228	260
6	SWATH	259	300	259	312	257	312	255	312
7	SWATH	299	340	311	340	309	340	307	340
8	SWATH	339	380	339	380	337	380	335	380
9	SWATH	379	420	379	420	377	420	375	420
10	SWATH	419	460	419	460	417	460	415	460
11	SWATH	459	500	459	511	457	511	455	511
12	SWATH	499	540	510	540	508	540	506	540
13	SWATH	539	580	539	580	537	580	535	580
14	SWATH	579	620	579	620	577	620	575	620
15	SWATH	619	660	619	672	617	672	615	672
16	SWATH	659	690	671	690	669	690	667	690

Table S3: Inclusion precursors covered in the ^{13}C labeling MRM^{HR} acquisition method

Compound ID	Group Name	Precursor Ion (Da)	TOF Start Mass (Da)	TOF Stop Mass (Da)	Accumulation Time (sec)	DP (V)	CE (V)	CE Spread (V)	Retention Time(min)	Retention time tolerance(+/- sec)	Fragmentation mode	Time Bins to Sum	Channel1	Channel2	Channel3	Channel4
Glutamate	Carbon	146.05	40	160	0.03	-80	-30	20	4.75	20	CID	4	True	True	True	True
Glutamate_C1	Carbon	147.05	40	160	0.03	-80	-30	20	4.75	20	CID	4	True	True	True	True
Glutamate_C2	Carbon	148.05	40	160	0.03	-80	-30	20	4.75	20	CID	4	True	True	True	True
Glutamate_C3	Carbon	149.06	40	160	0.03	-80	-30	20	4.75	20	CID	4	True	True	True	True
Glutamate_C4	Carbon	150.06	40	160	0.03	-80	-30	20	4.75	20	CID	4	True	True	True	True
Glutamate_C5	Carbon	151.06	40	160	0.03	-80	-30	20	4.75	20	CID	4	True	True	True	True
GABA	Carbon	102.06	40	110	0.06	-80	-30	20	5.7	20	CID	4	True	True	True	True
GABA_C1	Carbon	103.06	40	110	0.06	-80	-30	20	5.7	20	CID	4	True	True	True	True
GABA_C2	Carbon	104.06	40	110	0.06	-80	-30	20	5.7	20	CID	4	True	True	True	True
GABA_C3	Carbon	105.07	40	110	0.06	-80	-30	20	5.7	20	CID	4	True	True	True	True
GABA_C4	Carbon	106.07	40	110	0.06	-80	-30	20	5.7	20	CID	4	True	True	True	True
Glycine	Carbon	74.02	40	80	0.06	-80	-30	20	5.11	20	CID	4	True	True	True	True
Glycine_C1	Carbon	75.03	40	80	0.06	-80	-30	20	5.11	20	CID	4	True	True	True	True
Glycine_C2	Carbon	76.03	40	80	0.06	-80	-30	20	5.11	20	CID	4	True	True	True	True
Cysteine	Carbon	120.01	40	125	0.06	-80	-30	20	4.06	20	CID	4	True	True	True	True
Cysteine_C1	Carbon	121.02	40	125	0.06	-80	-30	20	4.06	20	CID	4	True	True	True	True
Cysteine_C2	Carbon	122.02	40	125	0.06	-80	-30	20	4.06	20	CID	4	True	True	True	True
Cysteine_C3	Carbon	123.02	40	125	0.06	-80	-30	20	4.06	20	CID	4	True	True	True	True
Serine	Carbon	104.04	40	110	0.06	-80	-30	20	5.39	20	CID	4	True	True	True	True
Serine_C1	Carbon	105.04	40	110	0.06	-80	-30	20	5.39	20	CID	4	True	True	True	True
Serine_C2	Carbon	106.04	40	110	0.06	-80	-30	20	5.39	20	CID	4	True	True	True	True
Serine_C3	Carbon	107.05	40	110	0.06	-80	-30	20	5.39	20	CID	4	True	True	True	True
GSH	Carbon	306.08	50	320	0.03	-80	-30	20	4.56	20	CID	4	True	True	True	True
GSH_C1	Carbon	307.08	50	320	0.03	-80	-30	20	4.56	20	CID	4	True	True	True	True
GSH_C2	Carbon	308.08	50	320	0.03	-80	-30	20	4.56	20	CID	4	True	True	True	True
GSH_C3	Carbon	309.09	50	320	0.03	-80	-30	20	4.56	20	CID	4	True	True	True	True
GSH_C4	Carbon	310.09	50	320	0.03	-80	-30	20	4.56	20	CID	4	True	True	True	True
GSH_C5	Carbon	311.09	50	320	0.03	-80	-30	20	4.56	20	CID	4	True	True	True	True
GSH_C6	Carbon	312.10	50	320	0.03	-80	-30	20	4.56	20	CID	4	True	True	True	True
GSH_C7	Carbon	313.10	50	320	0.03	-80	-30	20	4.56	20	CID	4	True	True	True	True
GSH_C8	Carbon	314.10	50	320	0.03	-80	-30	20	4.56	20	CID	4	True	True	True	True
GSH_C9	Carbon	315.11	50	320	0.03	-80	-30	20	4.56	20	CID	4	True	True	True	True
GSH_C10	Carbon	316.11	50	320	0.03	-80	-30	20	4.56	20	CID	4	True	True	True	True
Aspartate	Carbon	132.03	50	140	0.03	-80	-30	20	4.76	25	CID	4	True	True	True	True
Aspartate_C1	Carbon	133.03	50	140	0.03	-80	-30	20	4.76	25	CID	4	True	True	True	True
Aspartate_C2	Carbon	134.04	50	140	0.03	-80	-30	20	4.76	25	CID	4	True	True	True	True
Aspartate_C3	Carbon	135.04	50	140	0.03	-80	-30	20	4.76	25	CID	4	True	True	True	True
Aspartate_C4	Carbon	136.04	50	140	0.03	-80	-30	20	4.76	25	CID	4	True	True	True	True
Glyceraldehyde-3-P	Carbon	168.99	50	175	0.03	-80	-30	20	5.15	30	CID	4	True	True	True	True
Glyceraldehyde-3-P_C1	Carbon	169.99	50	175	0.03	-80	-30	20	5.15	30	CID	4	True	True	True	True
Glyceraldehyde-3-P_C2	Carbon	171.00	50	175	0.03	-80	-30	20	5.15	30	CID	4	True	True	True	True
Glyceraldehyde-3-P_C3	Carbon	172.00	50	175	0.03	-80	-30	20	5.15	30	CID	4	True	True	True	True
NAD	Carbon	662.10	80	700	0.03	-80	-30	20	5.1	30	CID	4	True	True	True	True
NAD_C1	Carbon	663.11	80	700	0.03	-80	-30	20	5.1	30	CID	4	True	True	True	True
NAD_C2	Carbon	664.11	80	700	0.03	-80	-30	20	5.1	30	CID	4	True	True	True	True
NAD_C3	Carbon	665.11	80	700	0.03	-80	-30	20	5.1	30	CID	4	True	True	True	True
NAD_C4	Carbon	666.12	80	700	0.03	-80	-30	20	5.1	30	CID	4	True	True	True	True

NAD_C5	Carbon	667.12	80	700	0.03	-80	-30	20	5.1	30	CID	4	True	True	True	True
NAD_C6	Carbon	668.12	80	700	0.03	-80	-30	20	5.1	30	CID	4	True	True	True	True
NAD_C7	Carbon	669.13	80	700	0.03	-80	-30	20	5.1	30	CID	4	True	True	True	True
NAD_C8	Carbon	670.13	80	700	0.03	-80	-30	20	5.1	30	CID	4	True	True	True	True
NAD_C9	Carbon	671.13	80	700	0.03	-80	-30	20	5.1	30	CID	4	True	True	True	True
NAD_C10	Carbon	672.14	80	700	0.03	-80	-30	20	5.1	30	CID	4	True	True	True	True
NAD_C11	Carbon	673.14	80	700	0.03	-80	-30	20	5.1	30	CID	4	True	True	True	True
NAD_C12	Carbon	674.14	80	700	0.03	-80	-30	20	5.1	30	CID	4	True	True	True	True
NAD_C13	Carbon	675.15	80	700	0.03	-80	-30	20	5.1	30	CID	4	True	True	True	True
NAD_C14	Carbon	676.15	80	700	0.03	-80	-30	20	5.1	30	CID	4	True	True	True	True
NAD_C15	Carbon	677.15	80	700	0.03	-80	-30	20	5.1	30	CID	4	True	True	True	True
NAD_C16	Carbon	678.16	80	700	0.03	-80	-30	20	5.1	30	CID	4	True	True	True	True
NAD_C17	Carbon	679.16	80	700	0.03	-80	-30	20	5.1	30	CID	4	True	True	True	True
NAD_C18	Carbon	680.16	80	700	0.03	-80	-30	20	5.1	30	CID	4	True	True	True	True
NAD_C19	Carbon	681.17	80	700	0.03	-80	-30	20	5.1	30	CID	4	True	True	True	True
NAD_C20	Carbon	682.17	80	700	0.03	-80	-30	20	5.1	30	CID	4	True	True	True	True
NAD_C21	Carbon	683.17	80	700	0.03	-80	-30	20	5.1	30	CID	4	True	True	True	True
Ribose-5P	Carbon	229.01	50	240	0.03	-80	-30	20	5.02	30	CID	4	True	True	True	True
Ribose-5P_C1	Carbon	230.02	50	240	0.03	-80	-30	20	5.02	30	CID	4	True	True	True	True
Ribose-5P_C2	Carbon	231.02	50	240	0.03	-80	-30	20	5.02	30	CID	4	True	True	True	True
Ribose-5P_C3	Carbon	232.02	50	240	0.03	-80	-30	20	5.02	30	CID	4	True	True	True	True
Ribose-5P_C4	Carbon	233.03	50	240	0.03	-80	-30	20	5.02	30	CID	4	True	True	True	True
Ribose-5P_C5	Carbon	234.03	50	240	0.03	-80	-30	20	5.02	30	CID	4	True	True	True	True
UTP	Carbon	482.96	70	500	0.1	-80	-30	20	7.2	40	CID	4	True	True	True	True
UTP_C1	Carbon	483.96	70	500	0.1	-80	-30	20	7.2	40	CID	4	True	True	True	True
UTP_C2	Carbon	484.97	70	500	0.1	-80	-30	20	7.2	40	CID	4	True	True	True	True
UTP_C3	Carbon	485.97	70	500	0.1	-80	-30	20	7.2	40	CID	4	True	True	True	True
UTP_C4	Carbon	486.97	70	500	0.1	-80	-30	20	7.2	40	CID	4	True	True	True	True
UTP_C5	Carbon	487.98	70	500	0.1	-80	-30	20	7.2	40	CID	4	True	True	True	True
UTP_C6	Carbon	488.98	70	500	0.1	-80	-30	20	7.2	40	CID	4	True	True	True	True
UTP_C7	Carbon	489.99	70	500	0.1	-80	-30	20	7.2	40	CID	4	True	True	True	True
UTP_C8	Carbon	490.99	70	500	0.1	-80	-30	20	7.2	40	CID	4	True	True	True	True
UTP_C9	Carbon	491.99	70	500	0.1	-80	-30	20	7.2	40	CID	4	True	True	True	True
Uridine	Carbon	243.06	50	260	0.1	-80	-30	20	2.02	20	CID	4	True	True	True	True
Uridine_C1	Carbon	244.07	50	260	0.1	-80	-30	20	2.02	20	CID	4	True	True	True	True
Uridine_C2	Carbon	245.07	50	260	0.1	-80	-30	20	2.02	20	CID	4	True	True	True	True
Uridine_C3	Carbon	246.07	50	260	0.1	-80	-30	20	2.02	20	CID	4	True	True	True	True
Uridine_C4	Carbon	247.08	50	260	0.1	-80	-30	20	2.02	20	CID	4	True	True	True	True
Uridine_C5	Carbon	248.08	50	260	0.1	-80	-30	20	2.02	20	CID	4	True	True	True	True
Uridine_C6	Carbon	249.08	50	260	0.1	-80	-30	20	2.02	20	CID	4	True	True	True	True
Uridine_C7	Carbon	250.09	50	260	0.1	-80	-30	20	2.02	20	CID	4	True	True	True	True
Uridine_C8	Carbon	251.09	50	260	0.1	-80	-30	20	2.02	20	CID	4	True	True	True	True
Uridine_C9	Carbon	252.09	50	260	0.1	-80	-30	20	2.02	20	CID	4	True	True	True	True
IMP	Carbon	347.04	70	370	0.03	-80	-30	20	4.65	30	CID	4	True	True	True	True
IMP_C1	Carbon	348.04	70	370	0.03	-80	-30	20	4.65	30	CID	4	True	True	True	True
IMP_C2	Carbon	349.05	70	370	0.03	-80	-30	20	4.65	30	CID	4	True	True	True	True
IMP_C3	Carbon	350.05	70	370	0.03	-80	-30	20	4.65	30	CID	4	True	True	True	True
IMP_C4	Carbon	351.05	70	370	0.03	-80	-30	20	4.65	30	CID	4	True	True	True	True
IMP_C5	Carbon	352.06	70	370	0.03	-80	-30	20	4.65	30	CID	4	True	True	True	True
IMP_C6	Carbon	353.06	70	370	0.03	-80	-30	20	4.65	30	CID	4	True	True	True	True

IMP_C7	Carbon	354.06	70	370	0.03	-80	-30	20	4.65	30	CID	4	True	True	True
IMP_C8	Carbon	355.07	70	370	0.03	-80	-30	20	4.65	30	CID	4	True	True	True
IMP_C9	Carbon	356.07	70	370	0.03	-80	-30	20	4.65	30	CID	4	True	True	True
IMP_C10	Carbon	357.07	70	370	0.03	-80	-30	20	4.65	30	CID	4	True	True	True
Inosine	Carbon	267.07	50	280	0.06	-80	-30	20	2.87	20	CID	4	True	True	True
Inosine_C1	Carbon	268.08	50	280	0.06	-80	-30	20	2.87	20	CID	4	True	True	True
Inosine_C2	Carbon	269.08	50	280	0.06	-80	-30	20	2.87	20	CID	4	True	True	True
Inosine_C3	Carbon	270.08	50	280	0.06	-80	-30	20	2.87	20	CID	4	True	True	True
Inosine_C4	Carbon	271.09	50	280	0.06	-80	-30	20	2.87	20	CID	4	True	True	True
Inosine_C5	Carbon	272.09	50	280	0.06	-80	-30	20	2.87	20	CID	4	True	True	True
Inosine_C6	Carbon	273.09	50	280	0.06	-80	-30	20	2.87	20	CID	4	True	True	True
Inosine_C7	Carbon	274.10	50	280	0.06	-80	-30	20	2.87	20	CID	4	True	True	True
Inosine_C8	Carbon	275.10	50	280	0.06	-80	-30	20	2.87	20	CID	4	True	True	True
Inosine_C9	Carbon	276.10	50	280	0.06	-80	-30	20	2.87	20	CID	4	True	True	True
Inosine_C10	Carbon	277.11	50	280	0.06	-80	-30	20	2.87	20	CID	4	True	True	True
ATP	Carbon	505.99	70	600	0.1	-80	-30	20	7.1	40	CID	4	True	True	True
ATP_C1	Carbon	506.99	70	600	0.1	-80	-30	20	7.1	40	CID	4	True	True	True
ATP_C2	Carbon	508.00	70	600	0.1	-80	-30	20	7.1	40	CID	4	True	True	True
ATP_C3	Carbon	509.00	70	600	0.1	-80	-30	20	7.1	40	CID	4	True	True	True
ATP_C4	Carbon	510.00	70	600	0.1	-80	-30	20	7.1	40	CID	4	True	True	True
ATP_C5	Carbon	511.01	70	600	0.1	-80	-30	20	7.1	40	CID	4	True	True	True
ATP_C6	Carbon	512.01	70	600	0.1	-80	-30	20	7.1	40	CID	4	True	True	True
ATP_C7	Carbon	513.01	70	600	0.1	-80	-30	20	7.1	40	CID	4	True	True	True
ATP_C8	Carbon	514.02	70	600	0.1	-80	-30	20	7.1	40	CID	4	True	True	True
ATP_C9	Carbon	515.02	70	600	0.1	-80	-30	20	7.1	40	CID	4	True	True	True
ATP_C10	Carbon	516.02	70	600	0.1	-80	-30	20	7.1	40	CID	4	True	True	True
Adenosine	Carbon	266.09	50	280	0.06	-80	-30	20	1.72	20	CID	4	True	True	True
Adenosine_C1	Carbon	267.09	50	280	0.06	-80	-30	20	1.72	20	CID	4	True	True	True
Adenosine_C2	Carbon	268.10	50	280	0.06	-80	-30	20	1.72	20	CID	4	True	True	True
Adenosine_C3	Carbon	269.10	50	280	0.06	-80	-30	20	1.72	20	CID	4	True	True	True
Adenosine_C4	Carbon	270.10	50	280	0.06	-80	-30	20	1.72	20	CID	4	True	True	True
Adenosine_C5	Carbon	271.11	50	280	0.06	-80	-30	20	1.72	20	CID	4	True	True	True
Adenosine_C6	Carbon	272.11	50	280	0.06	-80	-30	20	1.72	20	CID	4	True	True	True
Adenosine_C7	Carbon	273.11	50	280	0.06	-80	-30	20	1.72	20	CID	4	True	True	True
Adenosine_C8	Carbon	274.12	50	280	0.06	-80	-30	20	1.72	20	CID	4	True	True	True
Adenosine_C9	Carbon	275.12	50	280	0.06	-80	-30	20	1.72	20	CID	4	True	True	True
Adenosine_C10	Carbon	276.12	50	280	0.06	-80	-30	20	1.72	20	CID	4	True	True	True
Glutamine	Carbon	145.06	40	155	0.03	-80	-30	20	5.01	20	CID	4	True	True	True
Glutamine_C1	Carbon	146.07	40	155	0.03	-80	-30	20	5.01	20	CID	4	True	True	True
Glutamine_C2	Carbon	147.07	40	155	0.03	-80	-30	20	5.01	20	CID	4	True	True	True
Glutamine_C3	Carbon	148.07	40	155	0.03	-80	-30	20	5.01	20	CID	4	True	True	True
Glutamine_C4	Carbon	149.08	40	155	0.03	-80	-30	20	5.01	20	CID	4	True	True	True
Glutamine_C5	Carbon	150.08	40	155	0.03	-80	-30	20	5.01	20	CID	4	True	True	True
a-Ketoglutarate	Carbon	145.01	50	155	0.06	-80	-30	20	3.88	25	CID	4	True	True	True
a-Ketoglutarate_C1	Carbon	146.02	50	155	0.06	-80	-30	20	3.88	25	CID	4	True	True	True
a-Ketoglutarate_C2	Carbon	147.02	50	155	0.06	-80	-30	20	3.88	25	CID	4	True	True	True
a-Ketoglutarate_C3	Carbon	148.02	50	155	0.06	-80	-30	20	3.88	25	CID	4	True	True	True
a-Ketoglutarate_C4	Carbon	149.03	50	155	0.06	-80	-30	20	3.88	25	CID	4	True	True	True
a-Ketoglutarate_C5	Carbon	150.03	50	155	0.06	-80	-30	20	3.88	25	CID	4	True	True	True
Citrate	Carbon	191.02	40	200	0.03	-80	-30	20	6.4	40	CID	4	True	True	True

Citrate_C1	Carbon	192.02	40	200	0.03	-80	-30	20	6.4	40	CID	4	True	True	True
Citrate_C2	Carbon	193.03	40	200	0.03	-80	-30	20	6.4	40	CID	4	True	True	True
Citrate_C3	Carbon	194.03	40	200	0.03	-80	-30	20	6.4	40	CID	4	True	True	True
Citrate_C4	Carbon	195.03	40	200	0.03	-80	-30	20	6.4	40	CID	4	True	True	True
Citrate_C5	Carbon	196.04	40	200	0.03	-80	-30	20	6.4	40	CID	4	True	True	True
Citrate_C6	Carbon	197.04	40	200	0.03	-80	-30	20	6.4	40	CID	4	True	True	True
Succinate	Carbon	117.02	40	125	0.06	-80	-30	20	3.13	25	CID	4	True	True	True
Succinate_C1	Carbon	118.02	40	125	0.06	-80	-30	20	3.13	25	CID	4	True	True	True
Succinate_C2	Carbon	119.03	40	125	0.06	-80	-30	20	3.13	25	CID	4	True	True	True
Succinate_C3	Carbon	120.03	40	125	0.06	-80	-30	20	3.13	25	CID	4	True	True	True
Succinate_C4	Carbon	121.03	40	125	0.06	-80	-30	20	3.13	25	CID	4	True	True	True
Fumarate	Carbon	115.00	20	125	0.06	-80	-30	20	4.3	25	CID	4	True	True	True
Fumarate_C1	Carbon	116.01	20	125	0.06	-80	-30	20	4.3	25	CID	4	True	True	True
Fumarate_C2	Carbon	117.01	20	125	0.06	-80	-30	20	4.3	25	CID	4	True	True	True
Fumarate_C3	Carbon	118.01	20	125	0.06	-80	-30	20	4.3	25	CID	4	True	True	True
Fumarate_C4	Carbon	119.02	20	125	0.06	-80	-30	20	4.3	25	CID	4	True	True	True
Malate	Carbon	133.01	40	140	0.07	-80	-30	20	4.2	25	CID	4	True	True	True
Malate_C1	Carbon	134.02	40	140	0.07	-80	-30	20	4.2	25	CID	4	True	True	True
Malate_C2	Carbon	135.02	40	140	0.07	-80	-30	20	4.2	25	CID	4	True	True	True
Malate_C3	Carbon	136.02	40	140	0.07	-80	-30	20	4.2	25	CID	4	True	True	True
Malate_C4	Carbon	137.03	40	140	0.07	-80	-30	20	4.2	25	CID	4	True	True	True
Pyruvate	Carbon	87.01	40	95	0.06	-80	-30	20	1.85	35	CID	4	True	True	True
Pyruvate_C1	Carbon	88.01	40	95	0.06	-80	-30	20	1.85	35	CID	4	True	True	True
Pyruvate_C2	Carbon	89.02	40	95	0.06	-80	-30	20	1.85	35	CID	4	True	True	True
Pyruvate_C3	Carbon	90.02	40	95	0.06	-80	-30	20	1.85	35	CID	4	True	True	True
Phosphoenolpyruvate	Carbon	166.98	50	175	0.03	-80	-30	20	5.4	25	CID	4	True	True	True
Phosphoenolpyruvate_C1	Carbon	167.98	50	175	0.03	-80	-30	20	5.4	25	CID	4	True	True	True
Phosphoenolpyruvate_C2	Carbon	168.98	50	175	0.03	-80	-30	20	5.4	25	CID	4	True	True	True
Phosphoenolpyruvate_C3	Carbon	169.99	50	175	0.03	-80	-30	20	5.4	25	CID	4	True	True	True
Lactate	Carbon	89.02	40	95	0.06	-80	-30	20	2.92	35	CID	4	True	True	True
Lactate_C1	Carbon	90.03	40	95	0.06	-80	-30	20	2.92	35	CID	4	True	True	True
Lactate_C2	Carbon	91.03	40	95	0.06	-80	-30	20	2.92	35	CID	4	True	True	True
Lactate_C3	Carbon	92.03	40	95	0.06	-80	-30	20	2.92	35	CID	4	True	True	True

Table S4: Inclusion precursors covered in the ^{15}N labeling MRM^{HR} acquisition method

Compound ID	Group Name	Precursor Ion (Da)	TOF Start Mass (Da)	TOF Stop Mass (Da)	Accumulation Time (sec)	DP (V)	CE (V)	CE Spread (V)	Fragmentation mode	Retention Time(min)	Retention time tolerance(+/-sec)	Time Bins to Sum	Channel1	Channel2	Channel3	Channel4
Glutamate	Nitrogen	146.05	40	160	0.08	-80	-30	20	4.75	20	CID	4	True	True	True	True
Glutamate_N1	Nitrogen	147.04	40	160	0.08	-80	-30	20	4.75	20	CID	4	True	True	True	True
GABA	Nitrogen	102.06	40	110	0.1	-80	-30	20	5.7	20	CID	4	True	True	True	True
GABA_N1	Nitrogen	103.05	40	110	0.1	-80	-30	20	5.7	20	CID	4	True	True	True	True
Glycine	Nitrogen	74.02	40	80	0.1	-80	-30	20	5.11	20	CID	4	True	True	True	True
Glycine_N1	Nitrogen	75.02	40	80	0.1	-80	-30	20	5.11	20	CID	4	True	True	True	True
Cysteine	Nitrogen	120.01	40	125	0.1	-80	-30	20	4.06	20	CID	4	True	True	True	True
Cysteine_N1	Nitrogen	121.01	40	125	0.1	-80	-30	20	4.06	20	CID	4	True	True	True	True
Serine	Nitrogen	104.04	40	110	0.1	-80	-30	20	5.39	20	CID	4	True	True	True	True
Serine_N1	Nitrogen	105.03	40	110	0.1	-80	-30	20	5.39	20	CID	4	True	True	True	True
GSH	Nitrogen	306.08	50	320	0.08	-80	-30	20	4.56	20	CID	4	True	True	True	True
GSH_N1	Nitrogen	307.07	50	320	0.08	-80	-30	20	4.56	20	CID	4	True	True	True	True
GSH_N2	Nitrogen	308.07	50	320	0.08	-80	-30	20	4.56	20	CID	4	True	True	True	True
GSH_N3	Nitrogen	309.07	50	320	0.08	-80	-30	20	4.56	20	CID	4	True	True	True	True
Aspartate	Nitrogen	132.03	50	140	0.08	-80	-30	20	4.76	25	CID	4	True	True	True	True
Aspartate_N1	Nitrogen	133.03	50	140	0.08	-80	-30	20	4.76	25	CID	4	True	True	True	True
NAD	Nitrogen	662.10	80	700	0.08	-80	-30	20	5.1	30	CID	4	True	True	True	True
NAD_N1	Nitrogen	663.10	80	700	0.08	-80	-30	20	5.1	30	CID	4	True	True	True	True
NAD_N2	Nitrogen	664.10	80	700	0.08	-80	-30	20	5.1	30	CID	4	True	True	True	True
NAD_N3	Nitrogen	665.09	80	700	0.08	-80	-30	20	5.1	30	CID	4	True	True	True	True
NAD_N4	Nitrogen	666.09	80	700	0.08	-80	-30	20	5.1	30	CID	4	True	True	True	True
NAD_N5	Nitrogen	667.09	80	700	0.08	-80	-30	20	5.1	30	CID	4	True	True	True	True
NAD_N6	Nitrogen	668.08	80	700	0.08	-80	-30	20	5.1	30	CID	4	True	True	True	True
NAD_N7	Nitrogen	669.08	80	700	0.08	-80	-30	20	5.1	30	CID	4	True	True	True	True
UTP	Nitrogen	482.96	70	500	0.1	-80	-30	20	7.2	40	CID	4	True	True	True	True
UTP_N1	Nitrogen	483.96	70	500	0.1	-80	-30	20	7.2	40	CID	4	True	True	True	True
UTP_N2	Nitrogen	484.96	70	500	0.1	-80	-30	20	7.2	40	CID	4	True	True	True	True
Uridine	Nitrogen	243.06	50	260	0.1	-80	-30	20	2.02	20	CID	4	True	True	True	True
Uridine_N1	Nitrogen	244.06	50	260	0.1	-80	-30	20	2.02	20	CID	4	True	True	True	True
Uridine_N2	Nitrogen	245.06	50	260	0.1	-80	-30	20	2.02	20	CID	4	True	True	True	True
IMP	Nitrogen	347.04	70	370	0.1	-80	-30	20	4.65	30	CID	4	True	True	True	True
IMP_N1	Nitrogen	348.04	70	370	0.1	-80	-30	20	4.65	30	CID	4	True	True	True	True
IMP_N2	Nitrogen	349.03	70	370	0.1	-80	-30	20	4.65	30	CID	4	True	True	True	True
IMP_N3	Nitrogen	350.03	70	370	0.1	-80	-30	20	4.65	30	CID	4	True	True	True	True
IMP_N4	Nitrogen	351.03	70	370	0.1	-80	-30	20	4.65	30	CID	4	True	True	True	True
Inosine	Nitrogen	267.07	50	280	0.1	-80	-30	20	2.87	20	CID	4	True	True	True	True
Inosine_N1	Nitrogen	268.07	50	280	0.1	-80	-30	20	2.87	20	CID	4	True	True	True	True
Inosine_N2	Nitrogen	269.07	50	280	0.1	-80	-30	20	2.87	20	CID	4	True	True	True	True
Inosine_N3	Nitrogen	270.06	50	280	0.1	-80	-30	20	2.87	20	CID	4	True	True	True	True
Inosine_N4	Nitrogen	271.06	50	280	0.1	-80	-30	20	2.87	20	CID	4	True	True	True	True
ATP	Nitrogen	505.99	70	600	0.1	-80	-30	20	7.1	40	CID	4	True	True	True	True
ATP_N1	Nitrogen	506.99	70	600	0.1	-80	-30	20	7.1	40	CID	4	True	True	True	True
ATP_N2	Nitrogen	507.98	70	600	0.1	-80	-30	20	7.1	40	CID	4	True	True	True	True
ATP_N3	Nitrogen	508.98	70	600	0.1	-80	-30	20	7.1	40	CID	4	True	True	True	True
ATP_N4	Nitrogen	509.98	70	600	0.1	-80	-30	20	7.1	40	CID	4	True	True	True	True
ATP_N5	Nitrogen	510.97	70	600	0.1	-80	-30	20	7.1	40	CID	4	True	True	True	True
Adenosine	Nitrogen	266.09	50	280	0.1	-80	-30	20	1.72	20	CID	4	True	True	True	True
Adenosine_N1	Nitrogen	267.09	50	280	0.1	-80	-30	20	1.72	20	CID	4	True	True	True	True
Adenosine_N2	Nitrogen	268.08	50	280	0.1	-80	-30	20	1.72	20	CID	4	True	True	True	True
Adenosine_N3	Nitrogen	269.08	50	280	0.1	-80	-30	20	1.72	20	CID	4	True	True	True	True
Adenosine_N4	Nitrogen	270.08	50	280	0.1	-80	-30	20	1.72	20	CID	4	True	True	True	True
Adenosine_N5	Nitrogen	271.07	50	280	0.1	-80	-30	20	1.72	20	CID	4	True	True	True	True
Glutamine	Nitrogen	145.06	40	155	0.08	-80	-30	20	5.01	20	CID	4	True	True	True	True
Glutamine_N1	Nitrogen	146.06	40	155	0.08	-80	-30	20	5.01	20	CID	4	True	True	True	True
Glutamine_N2	Nitrogen	147.06	40	155	0.08	-80	-30	20	5.01	20	CID	4	True	True	True	True

Table S5: Analysis of calibration curves by linear regression for targeted polar metabolites

Metabolite Name & Abbreviation		Monoisotopic peak quantification based on HILIC-Zeno MRM^{HR}: MS^1 TOF			Monoisotopic peak quantification based on HILIC-Zeno MRM^{HR}: MS^2 precursor ion		
		Range (µg/mL)	linear regression equation y=ax+b	Correlation coefficient r^2	Range (µg/mL)	linear regression equation y=ax+b	Correlation coefficient r^2
L-Glutamic acid	GLU	0.5-20	y = 0.09408x - 0.00654	0.9993	0.1-20	y = 0.09423x - 0.00184	0.99231
gamma-Aminobutyric acid	GABA	0.5-20	y = 0.01376x - 0.00321	0.9970	0.5-20	y = 0.02498x - 0.00722	0.98887
Glycine	GLY	2.5-20	y = 0.06750x - 0.02796	0.9705	0.1-20	y = 0.06265x - 0.00114	0.99284
Cysteine	CYS	0.5-20	y = 1.62624x - 0.13405	0.9849	0.5-20	y = 0.04268x - 0.00511	0.98631
Serine	SER	0.5-20	y = 1.85033x - 0.21612	0.9842	0.1-20	y = 0.15519x - 0.00468	0.99099
Glutathione	GSH	0.5-20	y = 0.65298x - 0.17207	0.9963	0.1-20	y = 0.19961x - 0.01335	0.99042
Oxidized glutathione	GSSG	1.25-20	y = 0.13221x - 0.07497	0.9957			
L-Aspartic acid	ASP	0.5-20	y = 0.06897x - 0.01162	0.9971	0.5-20	y = 0.08353x - 0.01169	0.98414
Glyceraldehyde 3-Phosphate	G3P	2.5-20	y = 0.13459x - 0.17471	0.9951	2.5-20	y = 0.05708x - 0.04520	0.97976
Quinolinic acid	QULN	0.5-10	y = 1.99410x - 0.56754	0.9932			
Nicotinic acid adenine dinucleotide	DNAD	0.1-20	y= 0.11626x - 0.00329	0.9993			
Nicotinamide adenine dinucleotide	NAD	0.1-20	y= 0.04911x + 0.00214	0.9978	0.1-20	y= 0.00661x - 0.00028	0.99223
Nicotinic acid	NAC	1.25-20	y= 0.49684x - 0.25695	0.9976			
Niacinamide	NCAM	0.5-7.5	y= 0.03137x + 0.46290	0.9783			
L-Tryptophan	TRP	0.1-15	y= 1.11278x - 0.02141	0.9969			
L-Kynurenine	KYNR	1.25-20	y= 0.25099x + 0.14489	0.9922			
D-Ribose 5-phosphate	R5P	1.25-20	y= 0.12687x + 0.05947	0.9959	0.5-20	y= 0.03181x + 0.00376	0.99025
Uridine 5'-monophosphate	UMP	1.25-20	y= 0.30577x + 0.14279	0.9924			
Uridine 5'-diphosphate	UDP	1.25-15	y= 0.18212x - 0.10722	0.9824			
Uridine triphosphate	UTP	0.5-20	y= 0.04053x - 0.00746	0.9972	0.5-20	y= 0.04263x - 0.00326	0.99768
Uridine	URI	1.25-20	y= 5.07060x + 2.06304	0.9936	1.25-20	y= 10.44443x + 4.55296	0.99138
L-Glutamine	GLN	2.5-20	y= 0.34789x - 0.45254	0.9916	1.25-20	y= 0.12971x - 0.07467	0.99017

Inosinic acid	IMP	0.5-20	y= 0.17864x + 0.04607	0.9974	0.5-20	y= 0.13977x + 0.03870	0.99557
Inosine	INS	0.5-20	y= 2.29697x + 0.53440	0.9964	0.5-20	y= 13.48598x + 3.15770	0.99449
Adenosine monophosphate	AMP	0.5-20	y= 0.21048x + 0.03594	0.9983			
Adenosine diphosphate	ADP	1.25-20	y= 0.19175x - 0.11881	0.9918			
Adenosine triphosphate	ATP	0.5-20	y= 0.07104x - 0.00830	0.9990	0.5-20	y= 0.07631x + 0.00275	0.99854
Adenosine	ADN	0.5-20	y= 0.53435x - 0.04505	0.9985	0.5-20	y= 0.77803x + 0.04799	0.99665
Guanosine monophosphate	GMP	0.5-20	y= 0.30406x + 0.02837	0.9973			
Guanosine diphosphate	GDP	1.25-20	y= 0.09374x - 0.04450	0.9898			
Guanosine triphosphate	GTP	1.25-20	y= 0.04653x - 0.01220	0.9972			
Guanosine	GSN	1.25-20	y= 1.49311x + 0.92908	0.9949			
Oxoglutaric acid	AKG	0.5-20	y= 0.37209x - 0.07267	0.9962	0.5-20	y= 0.07988x + 0.01483	0.99109
Citric acid	CIT	2.5-15	y= 0.0000112459x - 0.000020919	0.9885	2.5-15	y= 0.39052x - 0.68461	0.98252
Succinic acid	SUCC	0.5-20	y= 0.21359x - 0.01799	0.9994	0.1-20	y= 0.19293x + 0.00388	0.99613
Fumaric acid	FUM	0.5-15	y= 0.21057x - 0.01543	0.9937	0.5-15	y= 0.05153x + 0.00507	0.98513
L-Malic acid	MAL	0.5-15	y= 0.58386x - 0.21395	0.9922	0.5-15	y= 0.45951x - 0.16564	0.99381
Pyruvic acid	PYR	0.5-20	y= 0.12035x - 0.00952	0.9986	0.1-20	y= 0.14188x - 0.00227	0.995
Phosphoenolpyruvic acid	PEP	1.25-20	y= 0.06405x - 0.04292	0.9871	0.5-20	y= 0.01273x - 0.00236	0.9869
L-Lactic acid	LAC	0.5-20	y= 0.01475x + 0.00845	0.9953	0.5-20	y= 0.01674x + 0.00646	0.99327

Table S6. Reproducibility evaluation of ^{13}C mass isotopologue distribution for one sample set with no dilution (n = 3), twofold dilution (n = 3), and threefold dilution (n = 3) measured by HILIC-Zeno MRM^{HR} method

Isotopologue	DF_1x (n=3) protein content: 38.0ug	DF_2x (n=3) protein content: 19.0ug	DF_3x (n=3) protein content: 12.7ug	Mean ± SD	Inter CV %
GLU_$C_5H_9NO_4$_M0	0.25 ± 0.016	0.26 ± 0.019	0.29 ± 0.035	0.27 ± 0.030	11.2
GLU_$C_5H_9NO_4$_M1	0.03 ± 0.003	0.03 ± 0.003	0.03 ± 0.001	0.03 ± 0.003	9.5
GLU_$C_5H_9NO_4$_M2	0.18 ± 0.016	0.18 ± 0.024	0.20 ± 0.009	0.19 ± 0.018	9.5
GLU_$C_5H_9NO_4$_M3	0.12 ± 0.004	0.12 ± 0.010	0.11 ± 0.033	0.12 ± 0.018	15.4
GLU_$C_5H_9NO_4$_M4	0.21 ± 0.012	0.20 ± 0.016	0.19 ± 0.021	0.20 ± 0.017	8.6
GLU_$C_5H_9NO_4$_M5	0.21 ± 0.004	0.21 ± 0.016	0.18 ± 0.025	0.20 ± 0.023	11.4
aKG_$C_5H_6O_5$_M0	0.20 ± 0.010	0.18 ± 0.019	0.16 ± 0.015	0.18 ± 0.021	11.6
aKG_$C_5H_6O_5$_M1	0.05 ± 0.007	0.06 ± 0.004	0.06 ± 0.001	0.06 ± 0.009	15.4
aKG_$C_5H_6O_5$_M2	0.28 ± 0.017	0.30 ± 0.034	0.32 ± 0.011	0.30 ± 0.027	8.8
aKG_$C_5H_6O_5$_M3	0.11 ± 0.013	0.11 ± 0.010	0.10 ± 0.019	0.11 ± 0.013	11.7
aKG_$C_5H_6O_5$_M4	0.19 ± 0.022	0.18 ± 0.018	0.18 ± 0.010	0.18 ± 0.017	9.4
aKG_$C_5H_6O_5$_M5	0.17 ± 0.002	0.16 ± 0.019	0.17 ± 0.005	0.17 ± 0.011	6.7
GSH_$C_{10}H_{17}N_3O_6S$_M0	0.25 ± 0.016	0.24 ± 0.046	0.23 ± 0.03	0.24 ± 0.03	12.4
GSH_$C_{10}H_{17}N_3O_6S$_M1	0.06 ± 0.003	0.06 ± 0.009	0.07 ± 0.008	0.07 ± 0.007	10.9
GSH_$C_{10}H_{17}N_3O_6S$_M2	0.20 ± 0.021	0.19 ± 0.042	0.18 ± 0.039	0.19 ± 0.032	16.8
GSH_$C_{10}H_{17}N_3O_6S$_M3	0.09 ± 0.015	0.10 ± 0.011	0.10 ± 0.014	0.09 ± 0.012	12.3
GSH_$C_{10}H_{17}N_3O_6S$_M4	0.16 ± 0.016	0.14 ± 0.033	0.16 ± 0.016	0.15 ± 0.022	14.2
GSH_$C_{10}H_{17}N_3O_6S$_M5	0.12 ± 0.009	0.13 ± 0.026	0.13 ± 0.028	0.13 ± 0.020	16.0
GSH_$C_{10}H_{17}N_3O_6S$_M6	0.06 ± 0.005	0.07 ± 0.005	0.06 ± 0.004	0.06 ± 0.007	11.3
GSH_$C_{10}H_{17}N_3O_6S$_M7	0.04 ± 0.005	0.04 ± 0.008	0.05 ± 0.008	0.04 ± 0.009	21.2
GSH_$C_{10}H_{17}N_3O_6S$_M8	0.01 ± 0.001	0.01 ± 0.002	0.01 ± 0.002	0.01 ± 0.002	24.2
GSH_$C_{10}H_{17}N_3O_6S$_M9	0.01 ± 0.001	0.01 ± 0.003	0.01 ± 0.002	0.01 ± 0.002	15.6
GSH_$C_{10}H_{17}N_3O_6S$_M10	0 ± 0	0 ± 0	0 ± 0	0 ± 0	15.4
GLU_Frag$C_4H_9NO_2$_M0	0.27 ± 0.004	0.27 ± 0.019	0.27 ± 0.010	0.27 ± 0.011	4.1
GLU_Frag$C_4H_9NO_2$_M1	0.17 ± 0.007	0.17 ± 0.012	0.18 ± 0.004	0.17 ± 0.010	5.7
GLU_Frag$C_4H_9NO_2$_M2	0.12 ± 0.003	0.12 ± 0.005	0.12 ± 0.003	0.12 ± 0.003	2.8
GLU_Frag$C_4H_9NO_2$_M3	0.22 ± 0.008	0.22 ± 0.015	0.21 ± 0.002	0.22 ± 0.010	4.5
GLU_Frag$C_4H_9NO_2$_M4	0.22 ± 0.005	0.22 ± 0.010	0.22 ± 0.012	0.22 ± 0.009	4.3
aKG_Frag$C_4H_6O_3$_M0	0.26 ± 0.020	0.24 ± 0.021	0.23 ± 0.024	0.24 ± 0.022	8.9
aKG_Frag$C_4H_6O_3$_M1	0.14 ± 0.009	0.15 ± 0.020	0.15 ± 0.008	0.14 ± 0.012	8.2
aKG_Frag$C_4H_6O_3$_M2	0.13 ± 0.005	0.14 ± 0.013	0.13 ± 0.003	0.13 ± 0.008	5.6
aKG_Frag$C_4H_6O_3$_M3	0.23 ± 0.015	0.23 ± 0.006	0.23 ± 0.026	0.23 ± 0.015	6.8
aKG_Frag$C_4H_6O_3$_M4	0.24 ± 0.015	0.25 ± 0.009	0.25 ± 0.009	0.25 ± 0.011	4.4
GSH_Frag$C_5H_6NO_3$_M0	0.34 ± 0.008	0.34 ± 0.037	0.34 ± 0.012	0.34 ± 0.020	5.9
GSH_Frag$C_5H_6NO_3$_M1	0.06 ± 0.003	0.06 ± 0.002	0.05 ± 0.005	0.06 ± 0.003	6.1
GSH_Frag$C_5H_6NO_3$_M2	0.19 ± 0.010	0.18 ± 0.0106	0.19 ± 0.017	0.19 ± 0.013	7.1
GSH_Frag$C_5H_6NO_3$_M3	0.11 ± 0.012	0.12 ± 0.016	0.12 ± 0.005	0.11 ± 0.011	10.1
GSH_Frag$C_5H_6NO_3$_M4	0.16 ± 0.011	0.17 ± 0.010	0.15 ± 0.009	0.16 ± 0.011	6.6
GSH_Frag$C_5H_6NO_3$_M5	0.14 ± 0.006	0.14 ± 0.010	0.15 ± 0.012	0.14 ± 0.008	5.9

Table S7. Determination of isotopomers distribution of $^{13}C_2$-gluatamte according to the labeling pattern of specific fragments in MS^2 spectrum

sample	Ratio			Ratio		Fraction		
	Frag_1 m+0	Frag_1 m+1	Frag_1 m+2	M+2_ 1,2-$^{13}C_2$-Glutamate	M+2_ 3,4-$^{13}C_2$-Glutamate	M+2	M+2_ 1,2-$^{13}C_2$-Glutamate	M+2_3,4-$^{13}C_2$-Glutamate
Control_C13_1	0	0.67	0.33	0.67	0.33	0.18	0.12	0.06
Control_C13_2	0	0.68	0.32	0.68	0.32	0.19	0.13	0.06
Control_C13_3	0	0.69	0.31	0.69	0.31	0.18	0.13	0.06
Control_C13_4	0	0.66	0.34	0.66	0.34	0.18	0.12	0.06
Control_C13_5	0	0.68	0.32	0.68	0.32	0.2	0.14	0.06
Rotenone_C13_1	0.01	0.79	0.21	0.79	0.21	0.17	0.14	0.04
Rotenone_C13_2	0.01	0.79	0.2	0.79	0.2	0.19	0.15	0.04
Rotenone_C13_3	0.01	0.78	0.21	0.78	0.21	0.21	0.16	0.04
Rotenone_C13_4	0.01	0.78	0.21	0.78	0.21	0.2	0.16	0.04
Rotenone_C13_5	0.01	0.79	0.2	0.79	0.2	0.17	0.13	0.03

Table S8. Determination of isotopomers distribution of $^{13}C_2$-glutathione according to the labeling pattern of specific fragments in MS^2 spectrum

sample	Ratio			Fraction			
	Frag_1 m+0 (M+2_ $^{13}C_2$-Gly)	Frag_1 m+1 (M+2_ $^{13}C_1$-Gly+ $^{13}C_1$-Glu)	Frag_1 m+2 (M+2_ $^{13}C_2$-Glu)	M+2	M+2_ $^{13}C_2$-Gly	M+2_ $^{13}C_1$-Gly+ $^{13}C_1$-Glu	M+2_ $^{13}C_2$-Glu
Control_C13_1	0.16	0	0.84	0.2	0.03	0	0.17
Control_C13_2	0.17	0	0.83	0.21	0.03	0	0.17
Control_C13_3	0.15	0	0.85	0.19	0.03	0	0.16
Control_C13_4	0.15	0	0.85	0.16	0.02	0	0.13
Control_C13_5	0.14	0	0.85	0.17	0.02	0	0.14
Rotenone_C13_1	0.61	0.01	0.39	0.04	0.03	0	0.02
Rotenone_C13_2	0.57	0.01	0.42	0.05	0.03	0	0.02
Rotenone_C13_3	0.53	0.01	0.47	0.04	0.02	0	0.02
Rotenone_C13_4	0.53	0.01	0.46	0.04	0.02	0	0.02
Rotenone_C13_5	0.55	0.01	0.44	0.05	0.02	0	0.02